JGR Earth Surface

RESEARCH ARTICLE
10.1029/2020JF006023

Inferring Ice Fabric From Birefringence Loss in Airborne Radargrams: Application to the Eastern Shear Margin of Thwaites Glacier, West Antarctica

T. J. Young[1], D. M. Schroeder[2,3], T. M. Jordan[4], P. Christoffersen[1], S. M. Tulaczyk[5], R. Culberg[3], and N. L. Bienert[3]

[1]Scott Polar Research Institute, University of Cambridge, Cambridge, UK, [2]Department of Geophysics, Stanford University, Stanford, CA, USA, [3]Department of Electrical Engineering, Stanford University, Stanford, CA, USA, [4]Plymouth Marine Laboratory, Plymouth, UK, [5]Department of Earth and Planetary Sciences, University of California, Santa Cruz, CA, USA

Key Points:

- Birefringence loss induces wave-like patterning across non-polarimetric ice-penetrating radargrams
- Fabric at the Thwaites shear margin are consistent with a non-ideal horizontal pole aligned with surface strain
- Analysis of birefringent patterning can constrain azimuthal fabric strength and define present and potentially past shear margins

Supporting Information:

Supporting Information may be found in the online version of this article.

Correspondence to:

T. J. Young,
tjy22@cam.ac.uk

Citation:

Young, T. J., Schroeder, D. M., Jordan, T. M., Christoffersen, P., Tulaczyk, S. M., Culberg, R., & Bienert, N. L. (2021). Inferring ice fabric from birefringence loss in airborne radargrams: Application to the eastern shear margin of Thwaites Glacier, West Antarctica. *Journal of Geophysical Research: Earth Surface*, *126*, e2020JF006023. https://doi.org/10.1029/2020JF006023

Received 4 DEC 2020
Accepted 23 APR 2021

Abstract In airborne radargrams, undulating periodic patterns in amplitude that overprint traditional radiostratigraphic layering are occasionally observed, however, they have yet to be analyzed from a geophysical or glaciological perspective. We present evidence supported by theory that these depth-periodic patterns are consistent with a modulation of the received radar power due to the birefringence of polar ice, and therefore indicate the presence of bulk fabric anisotropy. Here, we investigate the periodic component of birefringence-induced radar power recorded in airborne radar data at the eastern shear margin of Thwaites Glacier and quantify the lateral variation in azimuthal fabric strength across this margin. We find the depth variability of birefringence periodicity crossing the shear margin to be a visual expression of its shear state and its development, which appears consistent with present-day ice deformation. The morphology of the birefringent patterns is centered at the location of maximum shear and observed in all cross-margin profiles, consistent with predictions of ice fabric when subjected to simple shear. The englacial fabric appears stronger inside the ice stream than outward of the shear margin. The detection of birefringent periodicity from non-polarimetric radargrams presents a novel use of subsurface radar to constrain lateral variations in fabric strength, locate present and past shear margins, and characterize the deformation history of polar ice sheets.

Plain Language Summary Preferential orientation of ice crystals (its "fabric") can make ice more deformable in certain directions. We have observed wave-like patterns in airborne radar images that do not represent internal layers, but rather the direction of ice crystal orientation across the eastern shear margin of Thwaites Glacier, West Antarctica. The fabric is consistent with the stresses and strains observed at the glacier surface. These patterns may locate other shear margins and historical locations of past fast glacier flow.

1. Introduction and Motivation

Fast-flowing ice accounts for the majority of ice mass discharge to the ocean from the Antarctic Ice Sheet (e.g., Rignot et al., 2011), with recent measurements indicating an accelerating trend particularly in the Amundsen Sea embayment (Gardner et al., 2018; Shepherd et al., 2018). Regions of fast flow are facilitated by basal slip at the ice-bed interface, and restrained by a combination of basal drag and lateral shear at the margins separating fast and slow moving ice (Minchew et al., 2018; Schoof, 2004). Shear margins, characterized by persistent and anomalously intense shear deformation over distances as little as several kilometers, are subject to frictional heating and fabric development, both processes which reduce the resistance to shear (Meyer et al., 2018). Frictional heating is well-understood as a key control on ice rheology due to the thermoviscous feedback that facilitates the development of temperate ice (Haseloff et al., 2015; Hindmarsh, 2004; Jacobson & Raymond, 1998; Kyrke-Smith et al., 2013; Meyer & Minchew, 2018; Suckale et al., 2014). However, fabric development remains poorly understood due to a lack of in-situ measurements and is usually incorporated into models simply as a scalar enhancement factor, despite its importance in enabling streaming flow (Echelmeyer et al., 1994; Minchew et al., 2018). Ice crystals, which deform more easily along their basal planes than along their crystallographic (*c*)-axes, gradually re-orient themselves to

minimize resistance to stress, resulting in alignment with the compressive axis. Hence, their crystal orientation fabric (COF) reflects the deformational history of the ice (Alley, 1988) and represents a physical control upon ice-flow enhancement (Gillet-Chaulet et al., 2005; Smith et al., 2017).

While the COF of ice sheets are often directly quantified through thin-section analyses from ice cores (e.g., Hansen & Wilen, 2002), the complex logistics of coring operations, as well as their scientific goals, have restricted the locations of these measurements to slow-flowing (<50 m a^{-1}) sections of ice sheets usually situated over domes and divides (e.g., Jouzel & Masson-Delmotte, 2010). As such, these cores likely do not represent glaciologically dynamic areas that experience higher and more variable strain (Elsworth et al., 2020). In lieu of this constraint, ice-penetrating radar has provided an alternative method to quantify bulk anisotropic COF patterns by exploiting the birefringence of polar ice, without the practical limitations of drilling (e.g., Hargreaves, 1977; Fujita et al., 2006; K. Matsuoka et al., 2012; Jordan et al., 2019; Young et al., 2020).

Polar ice behaves as a birefringent material due to an anisotropy in the dielectric permittivity of ice crystals, which affects the polarization and direction of electromagnetic waves that propagate through the medium (Hargreaves, 1977). In polycrystalline ice with a preferred orientation, an electromagnetic wave decomposes into two orthogonally oriented components that propagate at different phase velocities in each orientation. The resulting phase shift rotates the electric field and can cause polarization misalignment with linearly polarized antennas, resulting in power loss (Doake, 1981). Previous radar studies have utilized multi- and quadrature-polarization setups to observe and quantify COF, and have shown good agreement with measurements from thin section analyses at coincident ice core sites (Fujita et al., 2006; Eisen et al., 2007; Ershadi et al., 2021; Dall, 2010, 2021; K. Matsuoka et al., 2003, 2009; Li et al., 2018; Jordan et al., 2019; Jordan, Besson, et al., 2020; Young et al., 2020) as well as provided evidence of more complex fabric at sites with more dynamic flow regimes (K. Matsuoka et al., 2012; Brisbourne et al., 2019; Jordan, Schroeder, et al., 2020; Jordan, Martín, et al., 2020). In-situ observations of ice fabric have been crucial to understanding the stress patterns and behaviors of ice sheets over time and over large areas (e.g., Alley, 1988; Budd, 1972) and have provided constraints on the influence of crystal fabric on ice sheet flow (Azuma, 1994; Martín et al., 2009; Thorsteinsson et al., 2003).

Airborne radargrams occasionally display depth-periodic modulations in received power that overprint and crosscut traditional radiostratigraphy arising from density and conductivity variations. However, the physical significance of these artifacts has not yet been addressed. We have observed such features in data collected over the shear margins of the Northeast Greenland Ice Stream (NEGIS), the eastern shear margin of Thwaites Glacier, and deep ice in the vicinity of Dome C and the upper catchment of Byrd Glacier (Figure 1). These observations span four different radar systems operating at center frequencies ranging from 60 to 750 MHz, with collection dates ranging from 2009 to 2019 (Table 1). This common behavior across a diversity of systems and flights suggests that this depth-periodic pattern is neither an instrument artifact nor the result of external radio frequency interference, but is instead intrinsic to either common processing methods or the ice sheet itself. These fading patterns do not correlate with englacial layer slopes, nor are they caused by destructive interference during coherent stacking over steeply dipping layering, which manifests as lossy regions that often stretch to the bed across a significant portion (1/3 to 1/2) of the vertical ice column with variable distance along the radar transect, thereby hampering the detection of traditional radiostratigraphic layer signals (Castelletti et al., 2019; Holschuh et al., 2014).

These depth-periodic patterns were clearly visible in raw data after range compression, but before additional stacking or synthetic aperture processing. Neither stacking nor focusing improved the apparent power loss, suggesting that the observed periodic minima are not a processing artifact. The instantaneous Doppler frequencies (Culberg & Schroeder, 2020; MacGregor et al., 2015) remained clustered around zero within the area where the periodic patterning is observed, evidence that this pattern is also unlikely to be the result of rough interface scattering or clutter, both of which would show increased or decreased Doppler frequencies from the off-nadir returns. The most plausible explanation for these observed patterns is that of birefringence-induced periodic power loss (hereafter termed "birefringence loss").

If these layers are the result of birefringence loss, then the strength of the englacial fabric scales proportionally with the difference between orthogonal permittivity components and the speed of polarization rotation (Hargreaves, 1977, 1978; Doake, 1981). Here, the fabric strength of ice is defined as the degree of directional

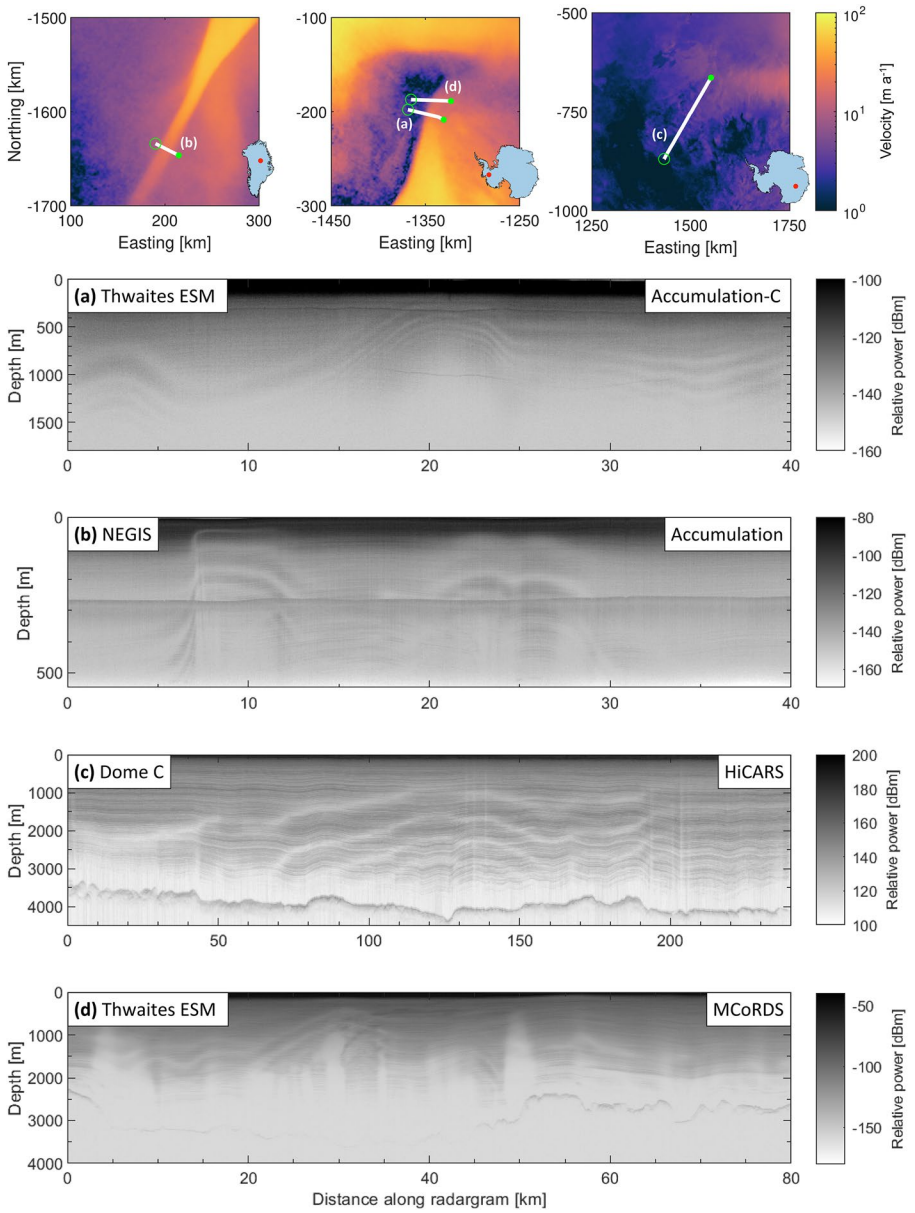

Figure 1. Radargram observations of birefringence-induced power loss (along-track depth-periodic wave-like patterns) at the eastern shear margin of Thwaites Glacier using the (a) University of Kansas CReSIS Accumulation-C and (d) MCoRDS radars; (b) the Northeast Greenland Ice Stream (NEGIS) using the CReSIS Accumulation radar; and (c) Dome C using the University of Texas Institute of Geophysics HiCARS radar. Abbreviations and specifications of each radar and their corresponding radargram are listed in Table 1. Panel (a) is the equivalent of Transect A (background of Figure 6b). The three top panels show the locations of (a) to (d) from start (hollow green circle) to end (filled green circle) over maps of ITS_LIVE surface velocity (Gardner et al., 2018) projected using WGS84 NSIDC Polar Stereographic North (for Greenland) or South (for Antarctica). Note the differences in scales between each panel. ESM, Eastern Shear Margin; HiCARS, High Capability Radar Sounder; MCoRDS, Multichannel Coherent Radar Depth Sounder; NEGIS, Northeast Greenland Ice Stream.

COF anisotropy comprising the englacial fabric, and the speed of polarization rotation refers to the rate at which the electric field of a radar wave rotates as it travels through a birefringent medium such as polar ice (Figure 2). This relationship in turn dictates the distance between successive local minima in received power due to birefringence loss through depth (hereafter termed "periodic birefringence-induced minima" or "birefringent minima") (K. Matsuoka et al., 2012). As a result, the wavelength of the resultant periodic birefringent minima indicates depth-averaged fabric strength, where the fast-time (the time measurement

Table 1
Properties of Non-Polarimetric Radars That Have Produced Radargrams With Birefringence-Induced Periodic Power Loss

Radar system	Accumulation-C	Accumulation	HiCARS	MCoRDS
Location	Thwaites ESM, Antarctica	NEGIS, Greenland	Dome C, Antarctica	Thwaites ESM, Antarctica
Center frequency (bandwidth) [MHz]	750 (300)	750 (320)	60 (15)	190 (50)
Pulse width [μs]	2.048	2	1	1/3/10[a]
Acquisition date (UTC)	January 29, 2019	April 4, 2012	December 22, 2009	November 9, 2016
Antenna type	Vivaldi	Planar array of elliptical dipoles	Dipole array	Dipole array
Antenna elements	4	8	2	6
Reference	Arnold et al. (2020)	Rodriguez-Morales et al. (2014)	Peters et al. (2007)	Arnold et al. (2020)

This list is not meant to be exhaustive and simply provides examples from a variety of radar systems. The acquisition date corresponds to radargrams shown in panels (a)–(d) in Figure 1. All antennas are collinearly aligned within each radar system.

Abbreviations: ESM, Eastern Shear Margin; HiCARS, High Capability Radar Sounder; MCoRDS, Multichannel Coherent Radar Depth Sounder; NEGIS, Northeast Greenland Ice Stream.

[a]Multiple pulse lengths spliced together to create the output radargram.

within each individual radar pulse through depth) period of each birefringent minima is inversely proportional with fabric asymmetry (Fujita et al., 2006).

In this study, our aim was to determine the origin and form of traced birefringent minima, and to quantify the bulk-fabric strength of ice across processed radargrams collected from the 2018–2019 airborne geophysics survey over the eastern shear margin (ESM) of Thwaites Glacier. The survey was conducted using the Center for Remote Sensing of Ice Sheets (CReSIS) Accumulation-C 750 MHz radar. We observed these patterns to be vertically separated by 100–400 m and smoothly ascend and descend as they approach and leave the delineation of maximum shear strain (Figure 1a). Using an established polarimetric backscatter model

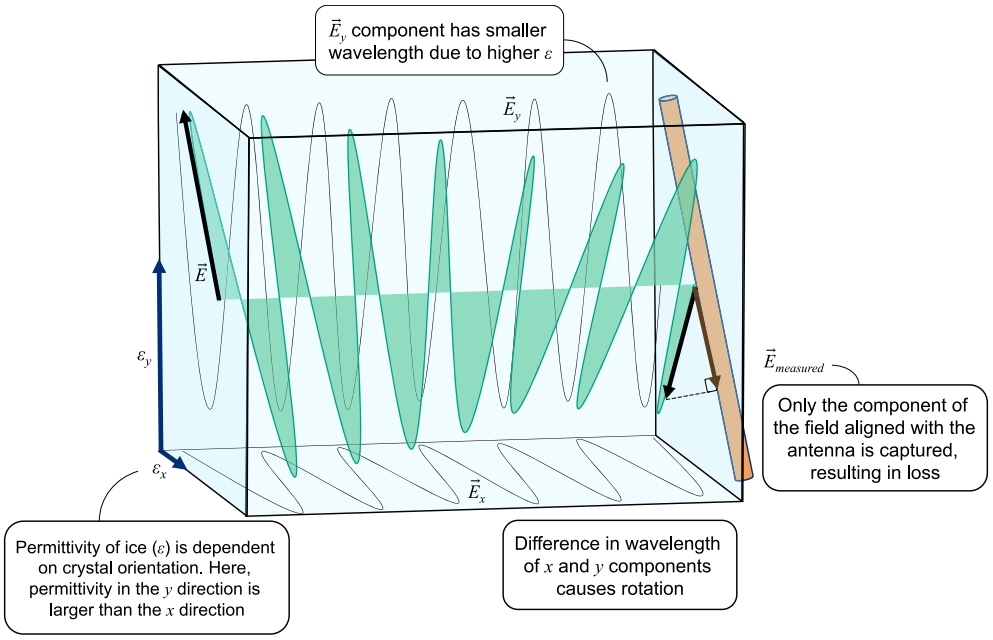

Figure 2. Schematic representation of the decomposition of a linearly polarized electromagnetic wave within polar ice (a birefringent medium), showing the general case where the antenna polarization plane is not aligned with the principal axes. Each wave component is orthogonally oriented along the primary planes of the electric field ($\vec{E}$) and therefore is aligned with the components of dielectric permittivity (ε). The differences in the two permittivity components produces a phase shift from the resulting differences in wavelengths, which causes polarization rotation and antenna mismatch manifested as an oscillatory pattern in power loss.

(Fujita et al., 2006) to quantify the observed birefringence loss in six radargrams, we quantify and reveal large-scale trends in fabric asymmetry and orientation, and from these results, infer the evolution of the ice crystal orientation fabric across the ESM as ice is subjected to varying levels of both pure and simple shear.

2. Theory of Electromagnetic Propagation in Birefringent Ice

2.1. Representation and Characterization of Ice Fabrics

The orientation of a single ice crystal can be described by the direction of its crystallographic (*c*-) axis, and the aggregate crystal orientation within polycrystalline ice comprises its crystal fabric (Woodcock, 1977). Fabrics evolve to develop characteristic patterns as a result of their deformation history based on the propensity of the *c*-axes to rotate toward the direction of maximum compressive stress (Azuma & Higashi, 1985; Castelnau et al., 1996). In general, minimal deformation will produce a near-isotropic (randomly distributed) fabric, such as those observed in young ice at the top of ice sheets (e.g., DiPrinzio et al., 2005; Fitzpatrick et al., 2014; Montagnat et al., 2014). At the center of an ideal ice dome, where vertical uniaxial compression is the sole form of deformation, the *c*-axes incline toward the vertical axis, resulting in a pole fabric (alternatively referred in other fabric studies as a "cluster") that strengthens with increasing depth as a result of increasing vertical compression (e.g., Azuma et al., 1999; Durand et al., 2007; Weikusat et al., 2017). At ice divides, where lateral tension exists from flow divergence, a vertical girdle pattern develops with the *c*-axes oriented orthogonal to the tensional axis (e.g., DiPrinzio et al., 2005; Fitzpatrick et al., 2014). Lastly, the fabric at ice stream margins has been hypothesized to be a non-ideal horizontal pole that enhances lateral shear (Jordan, Martín, et al., 2020).

The orientation of the fabric *c*-axes can be represented by a second-order orientation tensor with component eigenvalues that describe the relative concentration of *c*-axes projected along each of the three principal coordinate directions (eigenvectors), with higher eigenvalues indicating greater concentrations (Woodcock, 1977). Following previous studies that use radar to investigate ice fabric (Fujita et al., 2006): (i) the eigenvalues (a_1, a_2, a_3) represent the relative *c*-axis concentration along each principal coordinate direction (x_1, x_2, x_3); and (ii) these eigenvalues are normalized and have the properties $a_1 + a_2 + a_3 = 1$ and $a_1 < a_2 < a_3$.

Radar-sounding analyses of ice fabric generally needs to make a simplifying assumption that one of the fabric eigenvectors has to be aligned in the vertical direction. For the majority of fabric types (i.e., vertical girdles and vertical poles), the x_3 eigenvector is assumed to be vertically aligned with the x_1 and x_2 eigenvectors contained within the horizontal plane. With this convention, a random (isotropic) fabric is given by ($a_1 \approx a_2 \approx a_3 \approx 1/3$), a vertical pole fabric by ($a_1 \approx a_2 \ll a_3$), and a vertical girdle fabric by ($a_1 \ll a_2 \approx a_3$). In areas of high lateral shear, x_1 is instead assumed to be vertically aligned, with x_2 and x_3 representing the horizontal axes (Jordan, Martín, et al., 2020). Although not considered in this study, the presence of more complex fabric, such as the "horizontal partial girdle" detected in the trunk of Rutford Ice Stream by Smith et al. (2017) as a result of along-flow extension with lateral convergence, may also result in the x_2 eigenvector aligned in the vertical (with x_1 and x_3 aligned in the horizontal).

2.2. Dielectric Anisotropy and Birefringence of Polar Ice

In birefringent polar ice, the permittivity is described by a tensor rather than a scalar, meaning that the wave speed and wavelength are dependent on the wave's orientation relative to the permittivity's coordinate system (Woodcock, 1977). The electric field ($\vec{E}$) can be decomposed into two orthogonally oriented waves ($\vec{E}_x$ and $\vec{E}_y$) along the principal axes of the permittivity tensor (Hargreaves, 1977). Initially (at the ice surface), the wave components are in phase, but small differences in the respective dielectric permittivities along the planes that control their relative propagation speeds produce a relative phase shift between the components through depth that results in polarization rotation (K. Matsuoka et al., 2012) (Figure 2). Two-way birefringent propagation is additive (resulting in twice the net rotation) rather than compensating (resulting in net zero rotation) because the relative propagation speeds have the same relative difference independent of propagation direction. Linearly polarized antennas used for geophysical investigations typically only capture the component of the electric (E−) field aligned with the antenna, causing periodic power loss when the rotated E-field is not aligned with the antenna polarization plane, where the severity of the loss scales

with the relative angular displacement. This relationship between the strength of the received signal and the relative orientation of the antenna polarization plane has been reported since the earliest radio sounding surveys over polar ice (e.g., Bentley, 1975; Bogorodskiy et al., 1970; Jiracek, 1967). It was the amalgamation of these studies that determined polar ice to be birefringent at radio frequencies due to the apparent "depolari[zation] in the received echo" with respect to its azimuth (Woodruff & Doake, 1979).

For nadir measurements, the transverse (to propagation direction) polarized radio wave is sensitive to the fabric birefringence in the horizontal plane, which, expressed in terms of permittivity difference, is given by (Appendix of Fujita et al., 2006)

$$\Delta\varepsilon = \varepsilon_y - \varepsilon_x = \alpha\Delta\varepsilon'. \tag{1}$$

Here, the bulk (macroscopic) birefringence $\Delta\varepsilon$ is defined as the difference between the transverse components of the dielectric permittivity tensor ε_x and ε_y, $\Delta\varepsilon' = \varepsilon_{\parallel}^{'} - \varepsilon_{\perp}^{'}$ is the microscopic (crystal) birefringence with $\varepsilon_{\parallel}^{'}$ and $\varepsilon_{\perp}^{'}$ the dielectric permittivities for polarization planes parallel and perpendicular to the *c*-axis, and α represents the azimuthal fabric anisotropy (strength). At radar-sounding frequencies in the megahertz and gigahertz range, $\varepsilon_{\parallel}^{'}$ and $\varepsilon_{\perp}^{'}$ increase with temperature from ~3.15 to 3.19 and from ~3.12 to 3.16, respectively, for the range of expected ice temperatures (−60°–0°C), and $\Delta\varepsilon'$ varies from ~0.0339 to 0.0354 for the same frequency and temperature ranges (T. Matsuoka et al., 1997; Fujita et al., 2000, 2006). Although the dielectric anisotropy is small (1%–2% of the ice permittivity), the difference becomes noticeable at scales of tens to hundreds of meters in depth, as radio waves can only propagate within birefringent ice with an electric field along the two principal axes of the dielectric permittivity tensor (Fujita et al., 2006). For the majority of ordinary flow regimes, which include basal shear, divergent flow, and parallel flow (Alley, 1988), the x_3 axis is assumed to align with depth, and $\alpha = a_2 - a_1$. Most previous radar studies apply this assumption to characterize the strength and orientation of a vertical girdle (e.g., Fujita et al., 2006; K. Matsuoka et al., 2012; Jordan et al., 2019; Jordan, Schroeder, et al., 2020; Young et al., 2020). Here, low $a_2 - a_1$ values ($\alpha \leq 0.1$) represent azimuthally near-symmetrical fabrics such as isotropic or vertical pole fabrics, maximum values ($0.4 \leq \alpha \leq 0.5$) represent a near-ideal vertical girdle, and intermediate values ($0.1 < \alpha < 0.4$) represent the vertical girdle in its "non-ideal" or "partial" form (Kluskiewicz et al., 2017; Jordan et al., 2019; Jordan, Schroeder, et al., 2020; Jordan, Martín, et al., 2020; Young et al., 2020). The orientation of the vertical girdle can be determined by the direction of the x_2 eigenvector. If, however, the ice is subjected to intense lateral shear (Jordan, Martín, et al., 2020), then x_1 has been hypothesized to align with depth, and $\alpha = a_3 - a_2$. Our use of α is unrelated to the nomenclature of previous studies (e.g., Jordan et al., 2019; Li et al., 2018) that set α as the relative azimuthal angle. Under this assumption, the measured azimuthal fabric anisotropy characterizes the strength of a horizontal pole, and the orientation of the horizontal pole would then be determined by the direction of the x_3 eigenvector. In this case, an α value of 1 would represent an ideal (perfect) horizontal pole, with intermediate values representing its non-ideal form. In this study, we consider both vertical girdles (x_3 vertical) and horizontal poles (x_1 vertical) as sources of detected azimuthal fabric anisotropy, where its non-ideal state will be implicit in its α value. Regardless of the nomenclature used, polarimetric radar measurements detect the difference between the two horizontal eigenvalues irrespective of their ordering.

2.3. The Radar Power Equation for Anisotropic Ice

Radar sounding observations of terrestrial ice sheets are traditionally interpreted using a radar equation that represents the received power (P_r) in terms of system design (S), ice medium (I), and geometric spreading parameters (G) (e.g., Haynes et al., 2018; Ulaby et al., 1986). Conceptually, this relationship can be expressed as (Equation 1 in K. Matsuoka et al., 2012)

$$[P_r]_{dB} = [S]_{dB} + [I]_{dB} - [G]_{dB}, \tag{2}$$

where these parameters are given in the decibel scale ($[x]_{dB} = 10\log_{10}x$). A full argument formulated in K. Matsuoka et al. (2003, 2012) deduces S and G to be effectively polarization-independent, and that the depth variations from I are frequency-dependent. The effects of I on P_r can be further decomposed to (Equation 5 in K. Matsuoka et al., 2012)

$$[I]_{dB} = [\Gamma]_{dB} - [L]_{dB} - [B]_{dB}, \quad (3)$$

where Γ is the reflectivity, L is the integrated dielectric attenuation along the wave propagation path, and B is the power reduction relative to the isotropic ice caused by COF-induced birefringence. Γ is a conceptual representation of the Fresnel reflection coefficient, which is proportional to the scattering cross section and assumed specular (K. Matsuoka et al., 2003). If Γ is orientation-dependent, the scattering that arises from its reflectivity is considered to be anisotropic. Birefringence and anisotropic scattering are two related, but separate mechanisms that affect the polarization and azimuthal variation in the power of radar returns (Brisbourne et al., 2019). Because L is known to result in monotonic power decay (e.g., MacGregor et al., 2015; Stockham et al., 2016), only Γ and B are considered to be polarization-dependent, and therefore, affected by changes in COF. Specifically, Γ arises from anisotropic scattering as a consequence of abrupt and rapid depth variations in the anisotropy of permittivity in ice crystals, whereas B (associated with a smoothly varying fabric anisotropy) is a consequence of differences in dielectric permittivity along two axes perpendicular to the propagation direction (Drews et al., 2012). Although anisotropic scattering (Γ) and birefringence (B) typically occur simultaneously, only the latter is representative of the bulk COF of the incident ice column, where the strength of the measured fabric is inversely proportional to the wavelength of the observed mismatch (Figures 7 and 8 in Fujita et al., 2006).

Because anisotropic scattering in this study is prescribed as a relative term, we conceptualize reflectivity following Fujita et al. (2006) (their Equation 8) as $R = \left[\Gamma_y / \Gamma_x\right]_{dB}$, where R is the intensity ratio of the ($\vec{E}$-field) Fresnel reflection coefficient along the y-polarization plane relative to its equivalent in the x-polarization plane. As Equations 2 and 3 are additive, we express R in dB. In our models, we prescribe anisotropic scattering ratios of $R = 0$, 5, and 10 dB, which translates to the amount of anisotropic scattering in the y-polarization plane being 10^0 (i.e., equal to), $10^{1/2}$, and 10^1 times stronger than in the x-polarization plane.

2.4. Modeling Birefringence-Induced Power Loss

The polarimetric backscatter model formulated by Fujita et al. (2006) effectively relates the depth-periodicity of birefringent power minima to the polarimetric phase shift and the bulk ice azimuthal fabric strength. This model represents the orientation-dependence of received power (P_r) (Equations 9–12 in Fujita et al., 2006) to the radar received power equation (Equation 2) as a combination of anisotropic scattering (Γ, with its intensity ratio as R) and birefringence (B), the former as a scalar parameter that modulates the inequality in the scattering matrix (Equation 8 in Fujita et al., 2006) and the latter as α (Equation 1). The two-way polarimetric phase shift increases with ice depth and is given by (Equation 13 in Fujita et al., 2006)

$$\phi = \frac{4\pi f_c}{c}\int_{z_0}^{z}\left(\sqrt{\varepsilon_x(z)} - \sqrt{\varepsilon_y(z)}\right)dz, \quad (4)$$

where f_c is the central radar frequency, z_0 is an initial depth, c is the speed of light in vacuum, and ε are the dielectric permittivity tensor elements in the horizontal (x, y) plane. For small deviations about a mean (polarization-averaged) permittivity $\bar{\varepsilon}$ (where $\bar{\varepsilon} = \left(\varepsilon_x + \varepsilon_y\right)/2$), Equation 4 can be expressed through a first-order Taylor expansion as (Equation 12 in Jordan et al., 2019)

$$\phi = \frac{4\pi f_c}{c}\int_{z_0}^{z}\frac{\Delta\varepsilon(z)}{2\sqrt{\bar{\varepsilon}}}dz. \quad (5)$$

By rewriting Equation 4 as Equation 5, we are able to linearize the relationship between the phase shift, permittivity, and fabric strength. The theoretically predicted depth-averaged distance between successive birefringent minima over phase cycles of 2π radians can then be determined through Equations 1 and 5 within the polarimetric backscatter model as a function of horizontal fabric asymmetry (α). Because there also exists an inverse relationship between this periodicity and the radar center frequency (f_c) (Figure S2b), higher frequency radars are better suited to detect weaker ice fabric anisotropy than deep-penetrating radars (Figure 6 in Fujita et al., 2006).

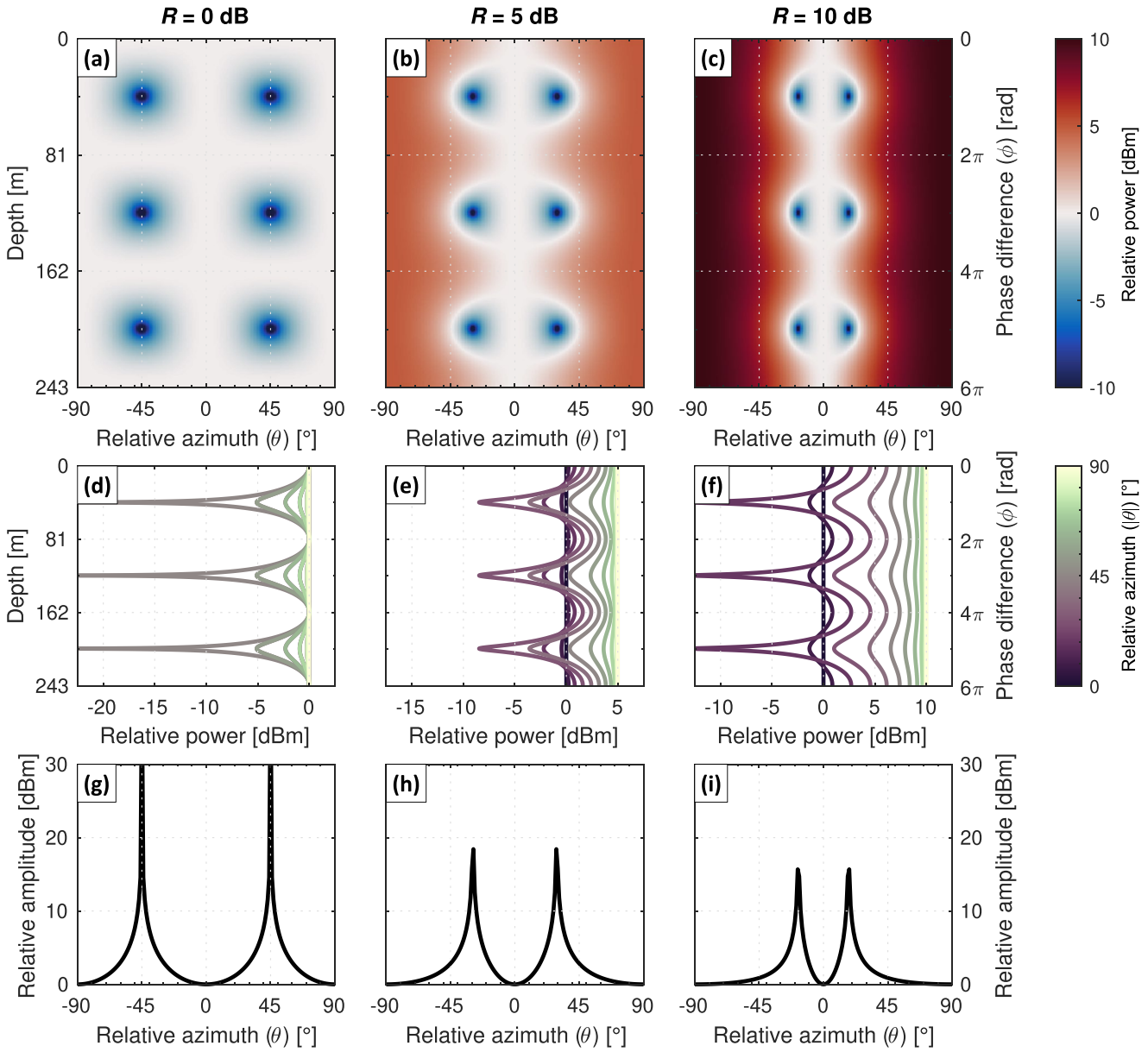

Figure 3. Modeled radar received power through depth and azimuth using the polarimetric backscatter model (Fujita et al., 2006) as a function of the anisotropic scattering ratio, using (a) $R = 0$ dB (isotropic scattering); (b) $R = 5$ dB (moderate anisotropic scattering); and (c) $R = 10$ dB (strong anisotropic scattering). (d), (e), and (f) show the modulation of received power at successive angles relative to the ice optic axis, extracted from the corresponding plots in (a), (b), and (c). (g), (h), and (i) show the maximum relative amplitude of each oscillatory pattern as a function of relative azimuth from corresponding plots in (d), (e), and (f), when the phase difference is at π, 3π, 5π, and so on. The depth-periodicity produced for all plots was determined using a center frequency of 750 MHz and an α value of 0.25.

Using the same polarimetric backscatter model, Fujita et al. (2006) (their Figure 5) determined that, for co-polarized antennas, extinction of the received signal occurs when the ice optic axis is aligned either parallel or perpendicular to the antenna polarization plane, and that periodic local power minima located off-axis are symmetric about the antenna's polarization plane (referred to in their paper as "co-polari[z]ation nodes"). These results are replicated in Figures 3a–3c with the antenna polarization plane centered at $\theta = 0°$ and using a radar central frequency of 750 MHz, the central frequency of the Accumulation-C radar. Additionally, Figure 3 reveals that the relative amount of prescribed anisotropic reflectivity (as a ratio R) affects the amplitude of theoretical birefringence loss, as well as on the azimuth of the ice optic axis relative to the antenna array polarization plane (the relative azimuth).

The detectability of birefringence-induced power minima in our study inherently depends on this specific relationship. In the case where the ice medium reflects isotropically (i.e., $R = 0$, Figure 3a), birefringence-induced power loss will be most pronounced when the ice optic axis is at 45° from the principal axes of the medium (Figures 3d and 3g). If the ratio of anisotropic scattering is stronger parallel to than perpendicular to the antenna polarization plane (i.e., $R > 0$, Figures 3b and 3c), the observed periodic power loss is largely constrained to between 0° and 45° (Figures 3e, 3f, 3h and 3i). If the anisotropic scattering ratio is instead stronger in the orthogonal direction (i.e., $R < 0$), the periodic power loss is instead constrained to between 45° and 90° (Figure S5). Anisotropic scattering (Γ, with its ratio as R) typically occurs when there is some degree of birefringence (B). However, the former exerts only azimuthal rather than depth control, whereas the converse is true for the latter (Figures 7 and 8 in Fujita et al., 2006). While the azimuthal extinction of the radar returned power is shown to be independent of Γ, the theoretical amount of B is perceived to be greatest when the relative azimuth equals the abscissa of the co-polarization nodes, which shifts closer to the principal axis with increasing anisotropic scattering. Therefore, the amount of anisotropic scattering present in the system dictates the specific azimuths at which birefringence-induced power loss is most pronounced.

In summary, the depth-periodic loss in received power, as a representation of the polarization mismatch, is proportional to the strength of the horizontal fabric within the propagated medium. A fully polarimetric, or multi-polarization radar system is required to completely quantify the azimuthal and depth variations as a result of Γ and B. However, from the theory posed, we argue that a single-polarization radar is sufficient to estimate the azimuthal fabric strength from B at coarse depth resolutions if and when the orientation of the underlying crystal fabric relative to the antenna polarization plane is aligned with or close to the azimuthal abscissa of the co-polarization nodes. In other words, given a preferential azimuthal offset between the antenna's primary axes and the fabric orientation, periodic patterns of birefringence-induced power extinction (indicative of the bulk fabric strength of underlying ice) will be superimposed onto the radargrams.

3. Methods

3.1. Radar Surveying and Processing

During the 2018–2019 International Thwaites Glacier Collaboration (ITGC) field campaign, a suite of aerogeophysical data sets were collected on board a British Antarctic Survey (BAS) de Havilland DHC-6 Twin Otter aircraft. In this study, we investigate the subset of radio-echo sounding data that traverses the eastern shear margin (ESM) of Thwaites Glacier (Figures 4a–4c). Troughs in the basal topography bound all except one of Thwaites Glacier's six distinct tributaries, the exception being the ESM, which does not appear to be strongly controlled by the local bed topography nor other basal properties (Holt et al., 2006; MacGregor et al., 2013; Schroeder et al., 2016) (Figure 4). Within our study area, situated ~400 km upstream from the grounding line, the orientation of the shear margin is offset by ~30° from its underlying basal trough at its upstream end, and roughly follows the 1,200 m contour at its downstream end, where the basal trough is less prominent (Figures 4d–4f).

The radargrams analyzed in this study were collected on January 29, 2019 (line 2) using the Accumulation-C radar developed by the Center for Remote Sensing of Ice Sheets (CReSIS). The Accumulation-C radar is a chirped pulse system operating over the 600–900 MHz frequency range, corresponding to a center frequency of 750 MHz with a bandwidth of 300 MHz (Table 1). The radar used a single four-element Vivaldi antenna array installed on the nadir port opening of the Twin Otter aircraft. The array uses an H-plane configuration, with antennas evenly separated by 12.065 cm (4.75 inches) and with the antenna E-plane oriented in the along-track direction (Lewis, 2010; Rodriguez-Morales et al., 2014). The theoretical range (depth) resolution for ice and snow using these parameters is ~50 and ~65 cm, respectively (Rodriguez-Morales et al., 2014). All radargrams were processed using focused synthetic-aperture radar (SAR) processing to create "CSARP_standard" combined-gain products, which present only the returned power without phase information.

The displayed radargrams comprise six 40 km sections (Transects A to F) of the flight line orthogonally (±10°) crossing the ESM (Figure 4). Each radargram is centered at the location of minimum shear strain (maximum shear magnitude), which serves as our definition for the shear margin center. Transects are

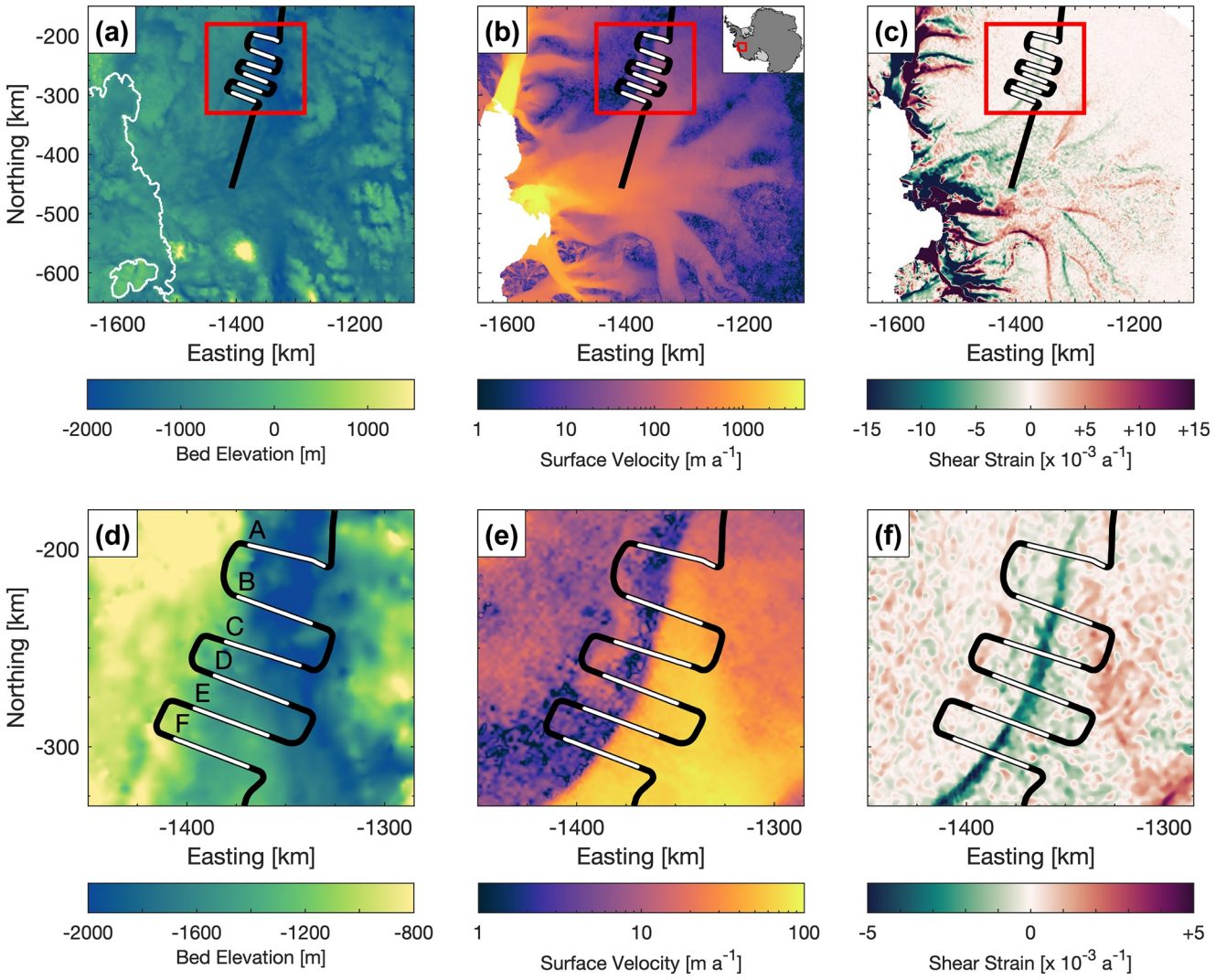

Figure 4. Spatial extent of Thwaites Glacier using maps of (a) BedMachine Antarctica v1 basal topography (Morlighem et al., 2020); (b) ITS_LIVE surface velocity (Gardner et al., 2018); and (c) lateral shear strain as calculated from (b), with positive-negative (red-green) values indicating counterclockwise-clockwise simple shear. ((d), (e), (f)) Magnification of ((a), (b), (c)) with respective spatial extents shown as a red box. The flight line is shown on all maps as a thick black line, with the six transects that form the data focus of this manuscript highlighted in white and labeled accordingly in (d). Location of Thwaites Glacier is shown in the inset on (b). Note the difference in color scales between ((a), (b), (c)) and ((d), (e), (f)). Strain rates are projected relative to the direction of ice flow (the strain axes being parallel and perpendicular to the flow direction). All panels were projected using WGS84 NSIDC Polar Stereographic South and made using Antarctic Mapping Tools (Greene et al., 2017).

separated from each other by ~25 km, with the exception of Transects A and B, which are separated by ~35 km. In all transects, the aircraft pitch and roll are observed to be minimal (Figure S1), and we, therefore, did not calculate additional error in birefringence estimates from off-nadir reflections (K. Matsuoka et al., 2009; Jordan et al., 2019; Jordan, Besson, et al., 2020). Surface velocities increased sigmoidally for all six transects crossing the shear margin (its domain defined, respectively, in Figures 6–11), with the majority (>90%) of the increase occurring within 5 km from the center of the shear margin. The ice was not observed to be flowing outwards of the shear margin (0–3 m a^{-1}), and on the other side, peak velocities along the transects within the ice stream ranged from ~25 m a^{-1} (Transect A, Figure 6d) to ~65 m a^{-1} (Transect F, Figure 11d). Although we noted no obvious consistency in basal topography across all transects, we observed the presence of slight (10–20 m deep) surface troughs in all but the uppermost transect (Transects B–F) consistent with similar observations made at the NEGIS (Riverman et al., 2019).

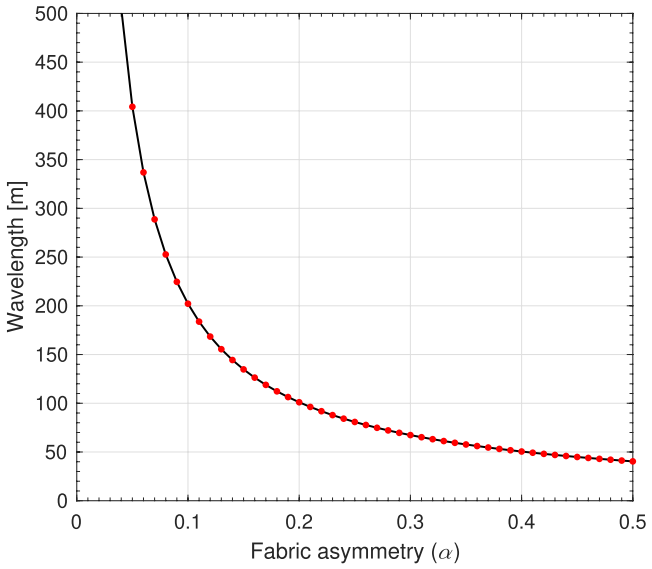

Figure 5. Relationship between horizontal fabric asymmetry ($\alpha = a_2 - a_1$ or $\alpha = a_3 - a_2$) and the wavelength between periodic birefringent minima in received power (distance between consecutive birefringent power minima), calculated with parameters $f_c = 750$ MHz, $R = 5$ dB, $\Delta\varepsilon' = 0.035$, and a model depth and azimuthal step of 1 m and 1°, respectively. Red points show calculations at an α resolution of 0.01.

3.2. Delineation of Periodic Birefringent Minima

Periodic birefringent power minima were semi-manually traced from identified local depth minima in the received power (Figure S3). The delineation of birefringent minima was threefold: (i) application of a two-dimensional convolution with the window dimension equivalent to 1/48 of the frame size (416 × 52 m in our study) to remove "traditional" reflection-induced layering that arises from changes in conductivity and permittivity; (ii) identification of local depth minima in received power with a minimum prominence of 15 dB at each distance step; and (iii) conversion of these minima into a continuous birefringence trace (Figure S3). In (iii), gaps in each pick were filled in through piecewise cubic interpolation and the resulting birefringent pattern was generated through fitting a Gaussian-weighted moving average over the picked minima corresponding to each manually identified trace. These processing steps were repeated for every radargram frame that constituted the airborne flight line, which may have resulted in slight discontinuities between neighboring frames.

3.3. Estimation of Azimuthal Fabric Asymmetry

Following Section 2.4, we estimated the bulk ice azimuthal fabric asymmetry α as a function of depth and orientation using the polarimetric backscatter model detailed in Fujita et al. (2006). Because the radar antennas were co-linearly aligned (Table 1), we did not apply azimuthal averaging to the resulting backscatter model results, as was the case in previous power-based analyses (K. Matsuoka et al., 2012; Brisbourne et al., 2019; Young et al., 2020). For our calculations, we used $f_c = 750$ MHz (Arnold et al., 2020), $\varepsilon'_{\parallel}$ and $\varepsilon'_{\perp}$ at 3.169 and 3.134, respectively, with $\Delta\varepsilon' = 0.035$ (T. Matsuoka et al., 1997), and a model depth and azimuthal step of 1 m and 1°, respectively. The wavelength of periodic birefringent minima was observed to decrease logarithmically with increasing fabric asymmetry, ranging from 450 m at an α value of 0.05 to ~50 m at 0.45 (Figure 5). These values of fabric asymmetry were calculated to the nearest 0.01. Although variations in frequency (f_c) and dielectric permittivity ($\Delta\varepsilon'$) will affect the relationship between ϕ and z (Figures S2b and S2c), the key source of uncertainty lies in the defined distance between successive birefringent minima. Because this distance represents the bulk-average of azimuthal fabric asymmetry within these bounds, we were unable to quantify this uncertainty without reference to in-situ crystal fabric observations.

Similar to Jordan, Martín, et al. (2020), our study considers both vertical girdles (x_3 vertical) and horizontal poles (x_1 vertical) as sources of azimuthal fabric asymmetry. We similarly apply their simplifications and make the default assumption that we detect the strength of a vertical girdle from the periodicity of birefringence loss (i.e., $\alpha = a_2 - a_1$) when analyzing cross-margin variations in birefringent patterning and fabric asymmetry (Section 4). Notwithstanding this assumption, we also identify the locations along each radargram where this assumption may not hold and the birefringent periodicity should instead indicate a horizontal pole (i.e., $\alpha = a_3 - a_2$). We discuss the results with respect to the flow direction, where x and y are aligned along and across flow, and z is positive with increasing depth.

From Section 2.4, we note that the choice of R is irrelevant so long as there is any amount of birefringence present. We also note that, from theory, birefringence-induced power loss will only manifest if the ice optic axis, and therefore, the principal axis system of the eigenvectors is not aligned with (parallel or perpendicular to) the antenna polarization plane (Fujita et al., 2006; K. Matsuoka et al., 2012). Given this limitation, we investigate the implications regarding the detectability of birefringence loss as a function of relative azimuth between the antenna polarization plane and the ice optic axis in Section 6.2.

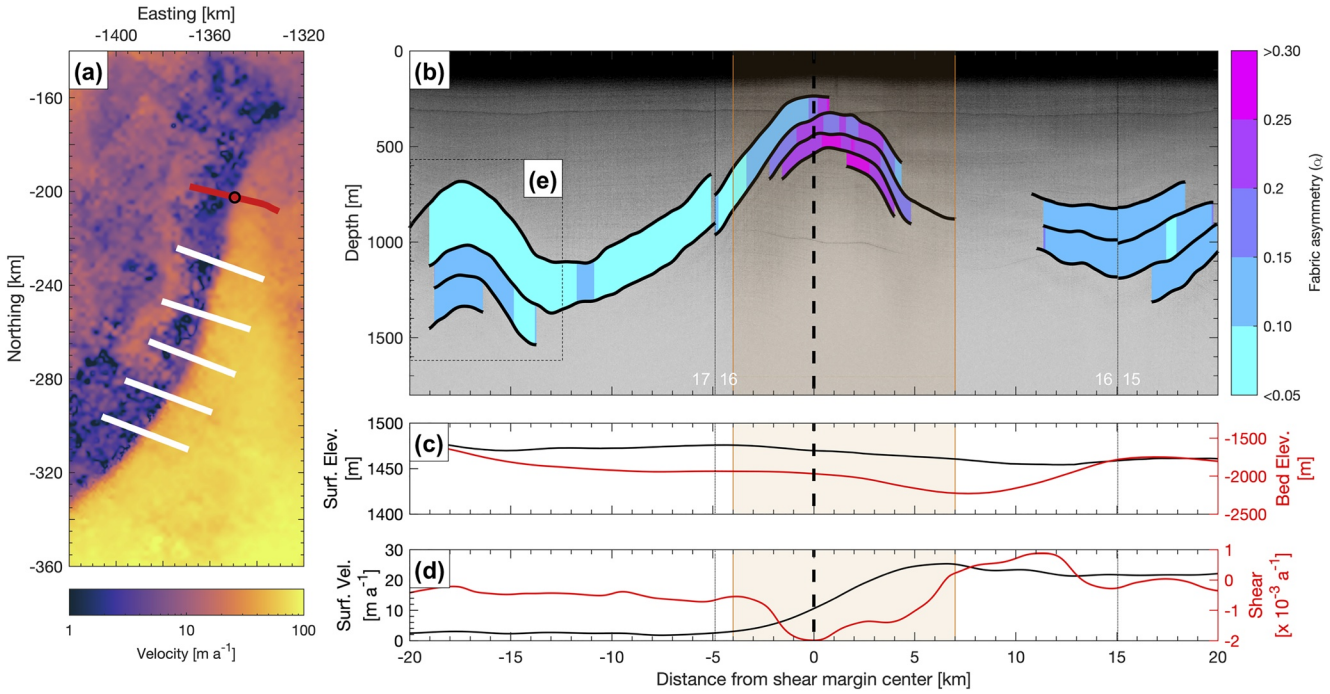

Figure 6. Quantification of azimuthal fabric asymmetry (locally depth-averaged between traced birefringent power minima) along Transect (a) (a) Location of radargram (red line) within the set of airborne transects (white lines), underlain by ITS_LIVE surface velocities (Gardner et al., 2018). Open black circle represents the estimated location of the shear margin center. (b) Radargram showing azimuthal fabric asymmetry (α) between traced birefringent layers, with original unmarked radargram shown in Figure S4. Radargram frame numbers are given in white. (c) Surface (black) and bed (red) elevation along radargram transect from BedMachine Antarctica v1 (Morlighem et al., 2020). (d) Surface velocity (black) and lateral shear strain (red) along radar transect derived from ITS_LIVE surface velocities (Gardner et al., 2018). (e) shows the location of an additional arcuate shaped birefringence feature that is thought to be the physical manifestation of a relic shear margin. The thick vertical dashed black line delineates the relative location of the shear margin as determined by the minimum in lateral shear strain (maximum shear magnitude), and the thin dotted lines show the start and ends of each 20 km-long image frame. Negative (positive) distance from the shear margin represents distance values outside (inside) the margin where the surface velocity slows down (speeds up). The domain shaded in orange highlights the zone of high lateral shear, where the model is likely to measure a horizontal pole (i.e., $\alpha = a_3 - a_2$) within these bounds, and a vertical girdle (i.e., $\alpha = a_2 - a_1$) outside these bounds. Radargram greyscale is the same as that of Figure 1a.

4. Cross-Margin Variations and Trends in Birefringent Patterning and Fabric Asymmetry

For each of the six radargram transects, we identified a suite of birefringent patterns that served as the basis for our analyses for their stratigraphic morphology and the resulting amount of azimuthal fabric asymmetry calculated from the distance between vertically consecutive birefringent minima (Figure S3). Figures 6–11 show the calculated fabric asymmetry between identified birefringent traces along the respective six transects A to F, with the transects ordered from up-to downglacier. In all six transects, we observed similar trends in both the lateral delineation of birefringence traces and their corresponding azimuthal fabric asymmetry. For our nomenclature, we describe ascending (descending) delineations to represent traced birefringent power minima that ascend toward (descend from) the ice surface with positive distance from the shear margin (left to right in Figures 6–11).

We observed in all six transects the ascent and descent of birefringent patterning as they approached and moved away from the center of the shear margin. The arcuate shape produced by the lateral variation in birefringence traces is centered about the point of maximum shear magnitude, with the shallowest detected birefringence trace situated at a depth of ~300 m in all transects. The lateral distribution of birefringence traces was observed to be asymmetric: the overall shape of the delineated traces outward of the shear margin (negative distances) are on average flatter and situated at lower depths than their counterparts inward of the shear margin (positive distances). We observed two visual exceptions to this trend. The first, shown in Transect A (Figure 6e), shows an additional ~500 m-high arch formation between 12 and 20 km outward of the shear margin (−20 to −12 km) that overprints the existing birefringent patterning. The second, shown 3–5 km inward of the margin center in Tran-

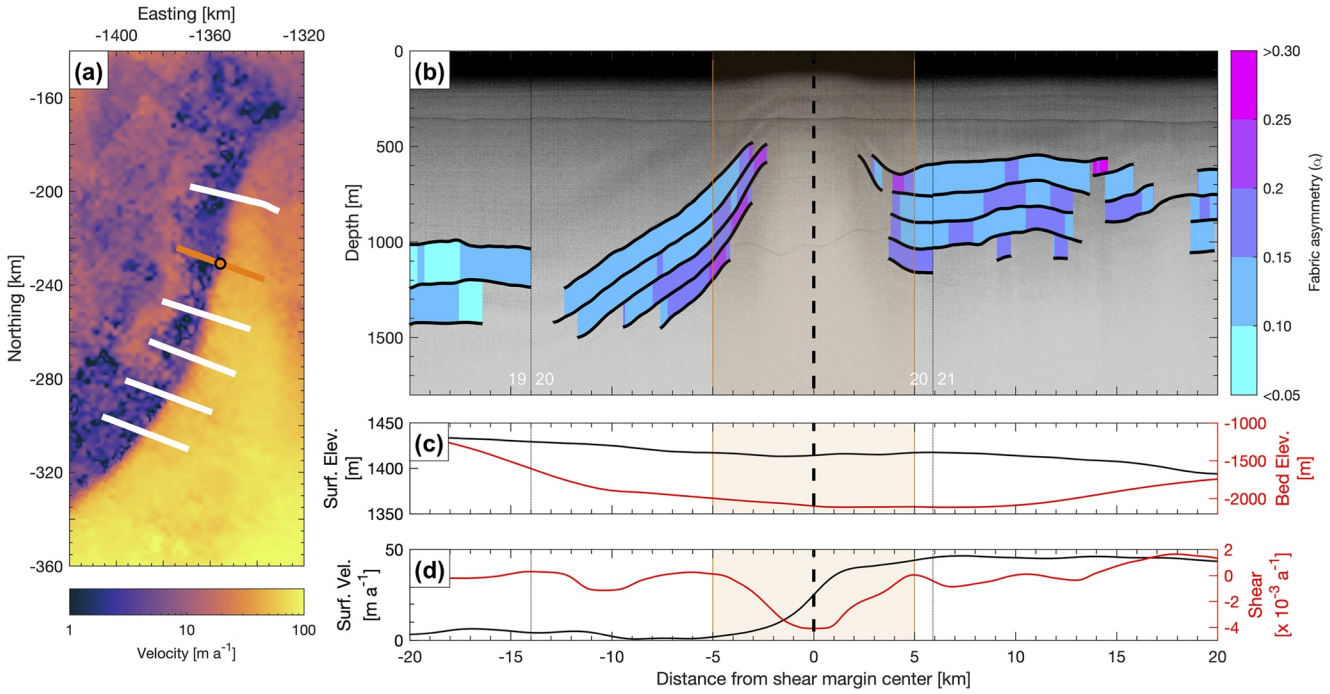

Figure 7. Quantification of azimuthal fabric asymmetry (locally depth-averaged between traced birefringent power minima) along Transect (b) Legends are identical with those for Figures 6a–6d with the exception of the transect color (orange) in panel (a). Unmarked radargrams are shown in Figure S4.

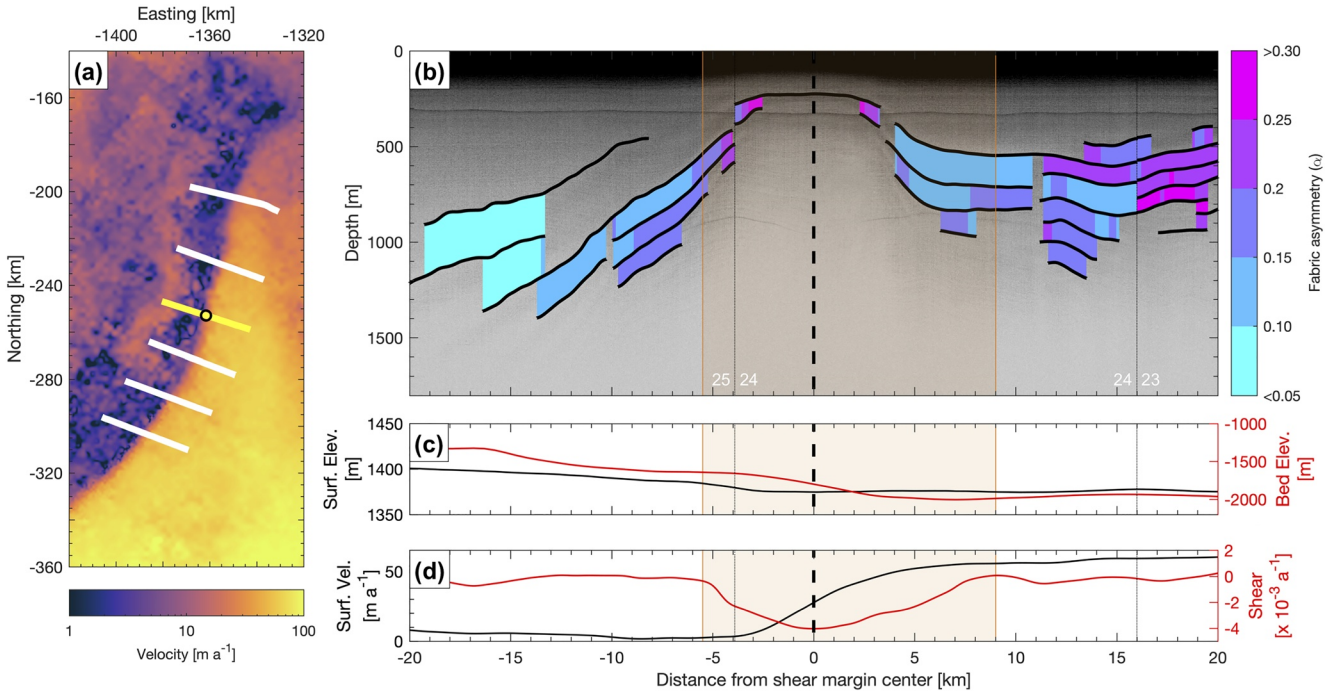

Figure 8. Quantification of azimuthal fabric asymmetry (locally depth-averaged between traced birefringent power minima) along Transect C. Legends are identical with those for Figures 6a–6d with the exception of the transect color (yellow) in panel (a). Unmarked radargrams are shown in Figure S4.

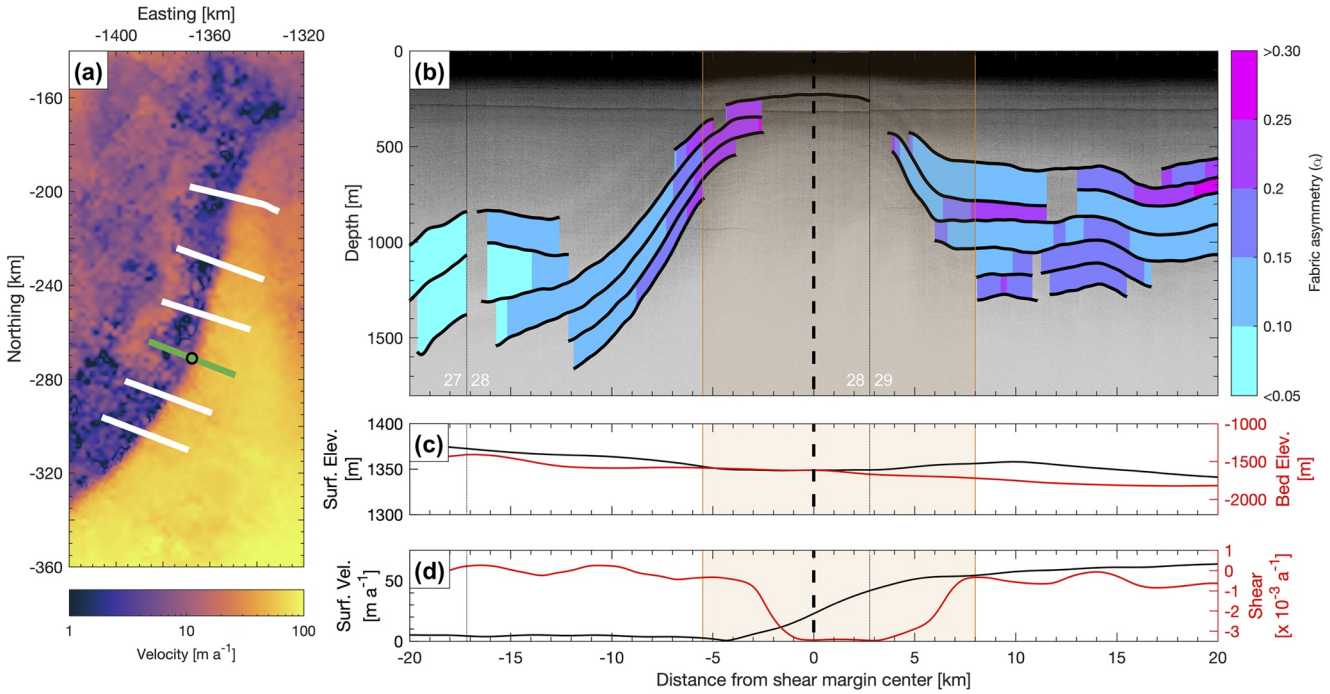

Figure 9. Quantification of azimuthal fabric asymmetry (locally depth-averaged between traced birefringent power minima) along Transect D. Legends are identical with those for Figures 6a–6d with the exception of the transect color (green) in panel (a). Unmarked radargrams are shown in Figure S4.

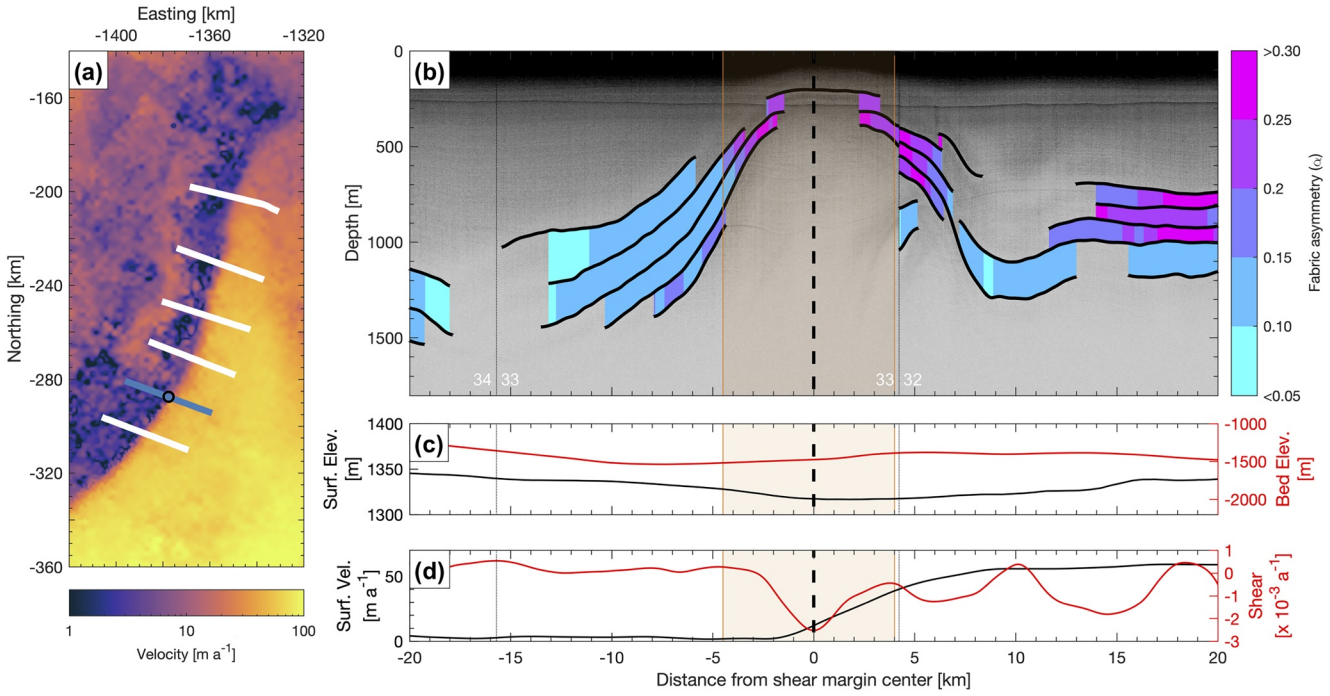

Figure 10. Quantification of azimuthal fabric asymmetry (locally depth-averaged between traced birefringent power minima) along Transect E. Legends are identical with those for Figures 6a–6d with the exception of the transect color (blue) in panel (a). Unmarked radargrams are shown in Figure S4.

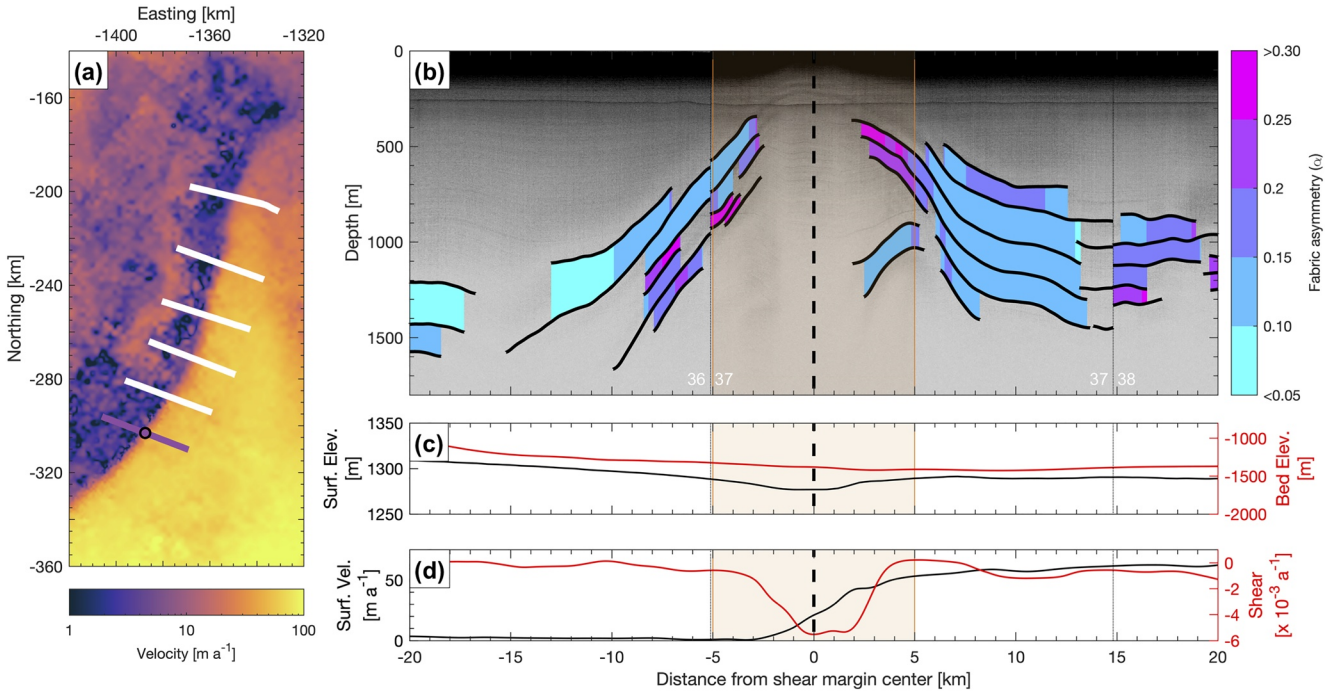

Figure 11. Quantification of azimuthal fabric asymmetry (locally depth-averaged between traced birefringent power minima) along Transect F. Legends are identical with those for Figures 6a–6d with the exception of the transect color (purple) in panel (a). Unmarked radargrams are shown in Figure S4.

sects E (Figure 10) and F (Figure 11), depicts the deepest delineated birefringent trace to sharply rise in depth at a rate of ~100 m km^{-1}, before either fading into the background noise (Transect E) or descending in conjunction with the rest of the other traces away from the margin center (Transect F). Away from the shear margin center, birefringence traces are observed at lower depths. In general, the identified birefringence traces are observed at lower depths on the slow side of the margin at 1,000–1,500 m, 20 km away from the margin center, than on the fast side where identified traces are situated at 600–1,200 m with little variability in depth. In all transects, we were able to delineate more traces at a wider range of depths inward than at or outward of the shear margin.

Figure 12 collates the slope of each identified birefringent trace and the calculated fabric asymmetry along all six transects. We observed that the dimensions of the arch form at the shear margin center are generally consistent across the six transects. We note that the arch form in Transect C (Figure 8b) is less prominent and wider than that of its counterparts (Figure 12b), resulting in a comparatively wider delineated shear margin boundary (Figure 12a). The shear margin boundaries for each transect (Figure 12a), defined by where the corresponding shear strain rates for each transect deviate from its baseline values inward or outward of the margin (Figures 6d–11d), roughly correspond to the points of maximum and minimum trace slopes for each transect (Figure 12b). These bounds delineate the shear margin from its periphery and determine whether the azimuthal fabric asymmetry (α) represents the anisotropy of a horizontal pole ($a_3 - a_2$) or a vertical girdle ($a_2 - a_1$), with the former assumption valid within these bounds and the latter outside these bounds.

We observed differences in α along all transects inwards of, outward of, and within the shear margin. Outward of the shear margin, α was observed to be uniformly low (<0.10), with values starting to increase between 10 and 15 km from the center of the shear margin, and the nature of this increase ranging from a linear (e.g., Transect C) to an exponential trend (e.g., Transect A) (Figure 12c). Fabric asymmetry values reach an absolute maximum ($0.25 < \alpha < 0.30$) at the margin center, before decreasing rapidly to a local minimum at ~8 km inside the ice stream. Trends in fabric asymmetry are not consistent beyond this distance, with the fabric strengths in some transects (e.g., Transects C, E, and F) increasing further inward into the shear margin, and remaining more or less constant in other transects (e.g., Transects A, B, and D). Overall, the girdle asymmetry was observed to be higher by 0.04–0.06 and more variable inward than outward of the shear margin (Figure 13b). We observed the pole asymmetry measured within the shear margin boundaries to be stronger than the girdle asymmetry outside the boundaries in all transects, with a difference of 0–0.08 (Figure 13a). In general, we

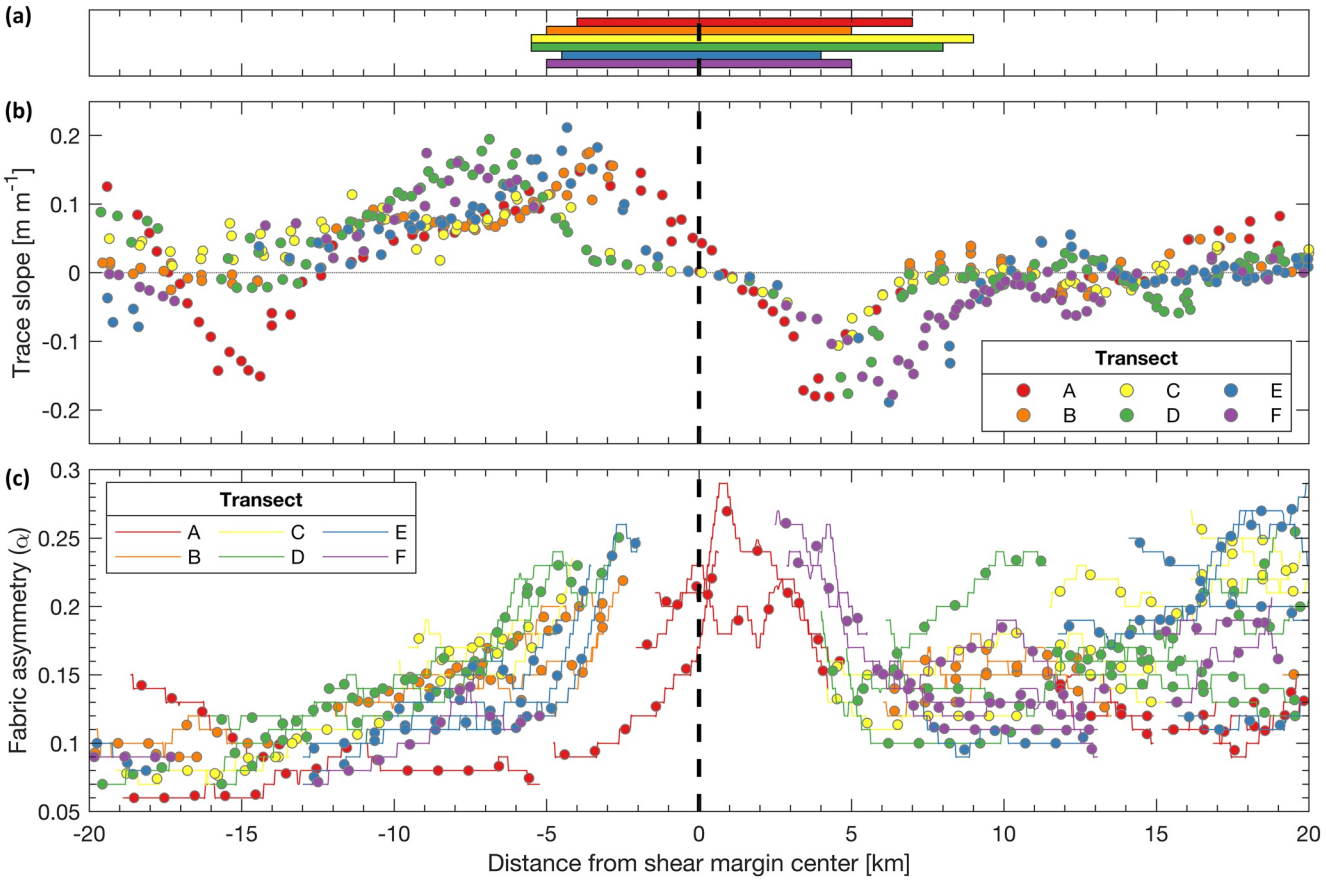

Figure 12. (a) Boundaries of shear margin along each of the six transects rounded to the nearest half-km, as defined by shear strain magnitudes shown in panel (d) of Figures 6–11. (b) Slope of birefringent minima trace with respect to the cross-flow distance for each of the 6 transects (dz/dy) at the Thwaites Glacier ESM. (c) Fabric asymmetry observed along each of the 6 transects across the ESM. The thick vertical dashed line represents the shear margin as determined by the location of minimum shear strain value along each transect. Dots represent the mean fabric asymmetry value at 1 km intervals and solid lines represent continuous fabric asymmetry segments between birefringent layers along each transect. Only segments and associated points longer than 2 km are shown. Note that the fabric asymmetry resolution in (c) is to the nearest 0.01. ESM, Eastern Shear Margin.

observed a positive correlation between spatially coincident variations in the slopes of birefringence traces and fabric asymmetry ($r^2 = 0.23$), where increases in the rate of change of bulk fabric asymmetry, defined by the incremental differences in calculated α values over the across-flow distance ($d\alpha/dy > 0$), are coincident with positive-sloping traces ($dz/dy > 0$), with the converse also being true (Figure 14). It then follows that changes in azimuthal fabric strength can be inferred from the morphology of birefringence traces: ascending traces correlate with an increasingly asymmetric fabric, and descending layers reflect the converse, reflecting a crystal fabric that tends toward isotropy, with the magnitude of the trace slope corresponding to a faster rate of change in fabric asymmetry. Though not obvious in Figure 14, Figure 12 reveals two notable exceptions to this correlation, which are located (i) −12 to −5 km outward of the shear margin center in Transect A (red); and (ii) 5–12 km inward of the margin center in Transect D (green).

5. Cross-Margin Fabric Development

Although the majority of in-situ observations of ice fabric are situated on ice domes and ice divides and represent only a small subset of the suite of deformation regimes occurring within dynamic ice flow features, the recent surge in the use of radar methods to estimate ice fabric (K. Matsuoka et al., 2012; Brisbourne et al., 2019; Jordan, Schroeder, et al., 2020; Jordan, Martín, et al., 2020) has confirmed theoretical and experimental results (Alley, 1988; Azuma & Higashi, 1985) relating fabric orientation to its deformational history in regions unsuitable for ice coring. While polarimetric radar studies generally show good alignment between the surface compression axis

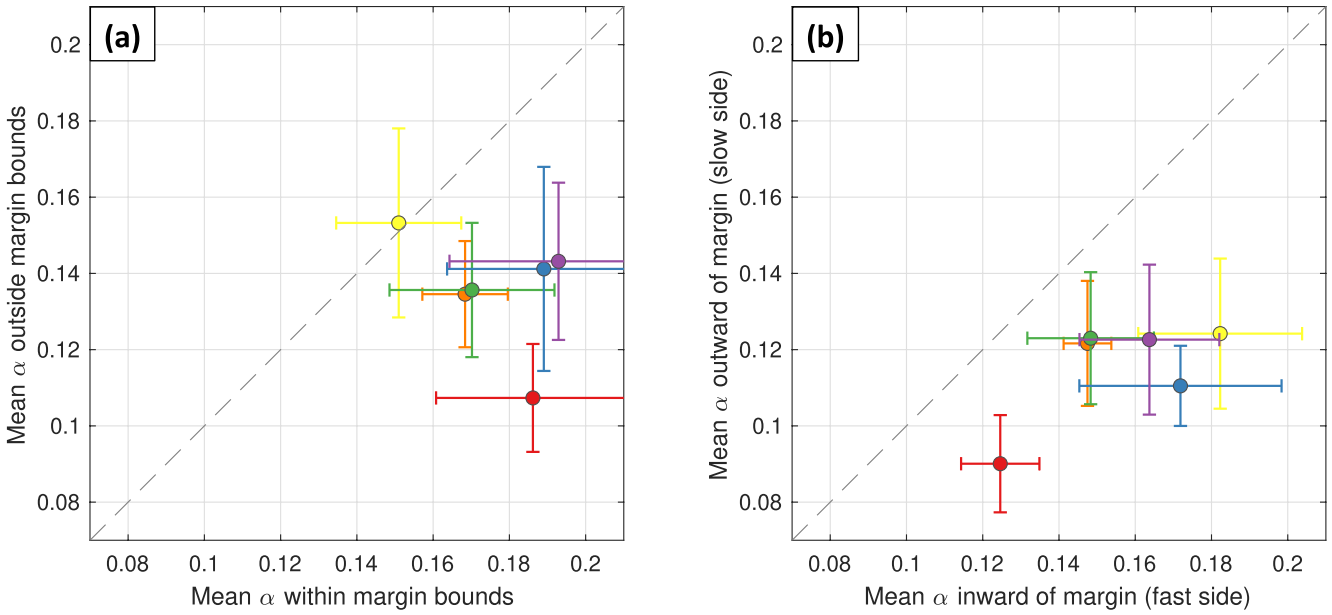

Figure 13. (a) Mean azimuthal fabric asymmetry (α) within and outside the shear margin boundaries; and (b) on each side of the shear margin (bottom row). Point colors follow Figures 6–12. Error bars represent the standard deviation of each quantity with respect to the axes labels. Gray dashed lines represent 1:1 relationships between the values on each axis.

and the azimuthal fabric orientation in shallower ice, the fabric orientation in deeper ice can be significantly misaligned with the surface strain field (K. Matsuoka et al., 2012; Brisbourne et al., 2019; Jordan, Martín, et al., 2020).

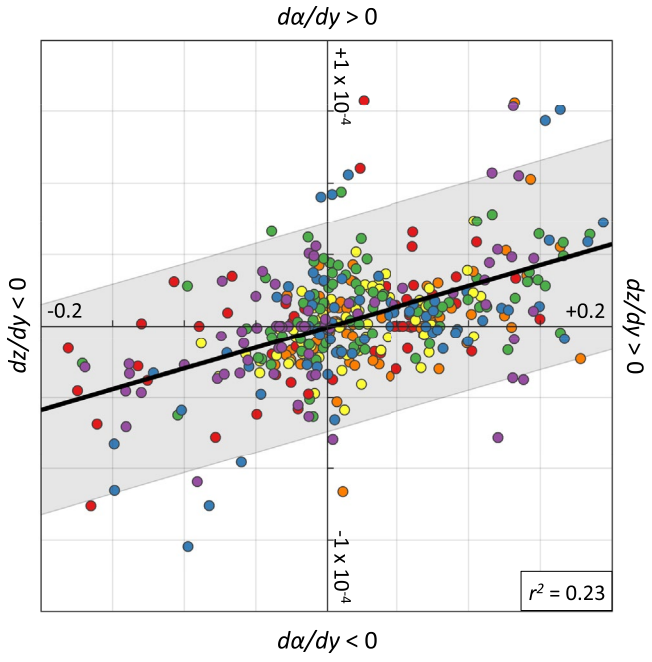

Figure 14. Relationship between the slope of birefringent layers (dz/dy) with the rate of change in azimuthal fabric asymmetry along each of the six transects ($d\alpha/dy$). dz/dy was calculated as the mean of the slopes of the upper and lower birefringent layers used to estimate the corresponding birefringence value. A linear regression was fitted to the colored points on each graph shown in Figure 12, with the corresponding standard error shown in gray. Point colors follow Figures 6–12.

In general, *c*-axis fabrics reflect and contribute to the cumulative strain and stress state in ice sheets: a vertical girdle fabric is consistent with lateral compression, while a horizontal pole fabric enhances lateral shear (Jordan, Martín, et al., 2020). The former corresponds well to the peripheries of the six radargram transects analyzed in this study. Within the ice stream, the imaged ice reveals COF that is on average more asymmetric (Figure 13b) and more variable (Figures 12b and 13b) than outside the shear margin. Low fabric strengths were universally inferred in all six transects at the outside periphery of the shear margin, where both surface flow (<3 m a^{-1}) and strain rates (~1 × 10^{-3} a^{-1}) are observed to be minimal ($a_2 - a_1 < 0.1$) (Figure 15a), which suggests a fabric that is near-isotropic in nature (Figure 16a). In stagnant ice with little observed divergence, any amount of horizontal anisotropy observed is likely to be a manifestation of deviatoric stresses acting in the horizontal plane (Alley, 1988). On the other side of the transect domains, where surface velocities increase downstream by more than twofold from 25 m a^{-1} at Transect A (Figure 6d) to 65 m a^{-1} at Transect F (Figure 11d), we observed increasingly asymmetric fabric across subsequent transects, with $a_2 - a_1$ values increasing from ~0.15 at Transect A to >0.25 farther downstream at Transects E and F (Figure 12c). These estimates suggest the development of a moderately strong azimuthally anisotropic fabric in the downstream reaches of our study area that is likely to be a vertical girdle (Figure 16c), in line with previous fabric deductions made in ice streams (Horgan et al., 2011; Jordan, Martín, et al., 2020). We note that the high variability observed in the fabric asymmetry values between transects (Figure 12c) may reflect the complex strain regime at the local scale (1–10 km; Figure 15a).

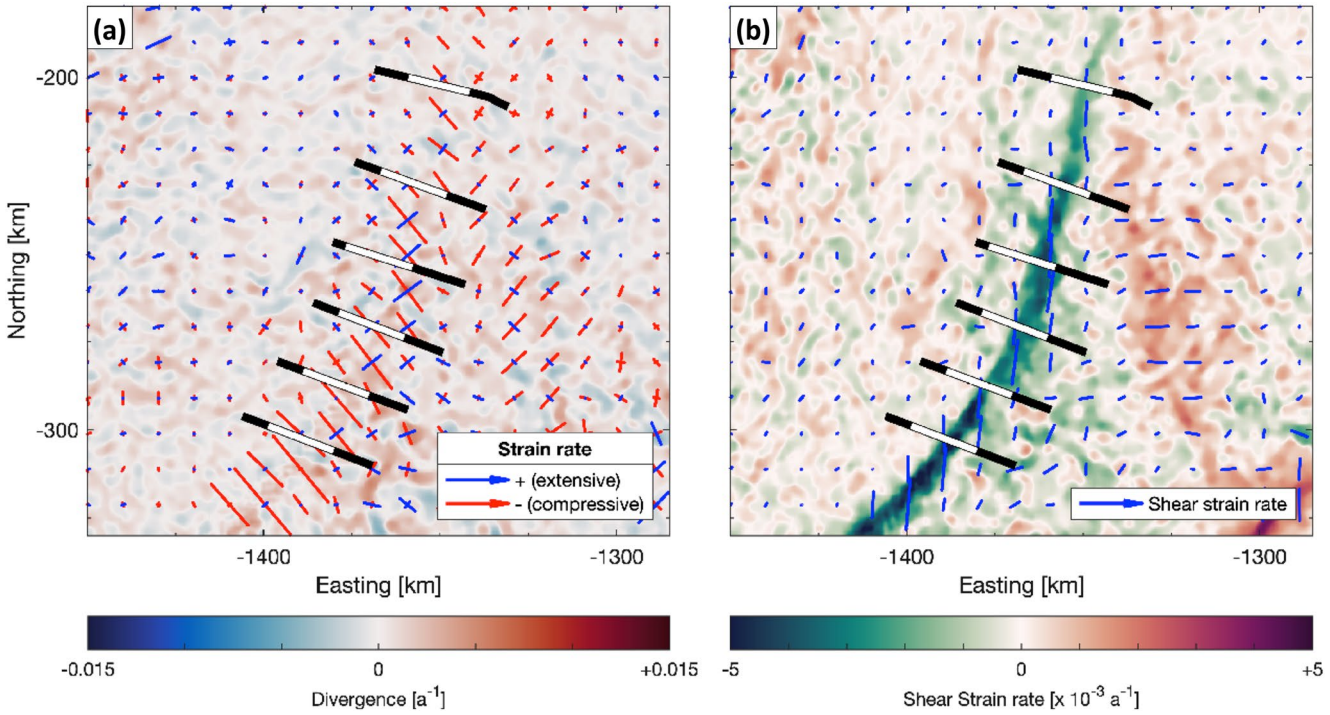

Figure 15. Magnitude and orientation of (a) principal surface strain rate components overlain on a map showing surface velocity magnitudes; and (b) shear strain overlain on a map showing lateral shear strain rate magnitudes and the shear plane orientation. The strain field is gridded at a resolution of 10 km, with the reference vector in the legends all representing a magnitude of 0.0025 a^{-1}. To smooth out any fine-scale heterogeneities, the strain fields were subjected to a 2-D peak convolution using a Gaussian low-pass filter. The six transects A–F (Figures 6–11) are shown as black lines, and the assigned boundaries of the shear margin within each transect (Figure 12) are highlighted in white. The spatial extents shown here are the same as that of Figures 4d–4f.

When fabric is subjected to simple shear and transverse compression, it tends toward a horizontal pole (Figure 16b) that is normal to the shear plane as suggested by experimental, modeling, and theoretical studies (e.g., Bouchez & Duval, 1982; Qi et al., 2019; Wilson & Peternell, 2011) with its orientation defined by the direction of the x_3 eigenvector. In a recent study that analyzed polarimetric ApRES radar returns along a transect approaching but not crossing the shear margin from the inside of Rutford Ice Stream, West Antarctica, Jordan, Martín, et al. (2020) observed the fabric (assumed to be a non-ideal horizontal pole) orientation to be azimuthally offset from the surface ice flow direction by 45°, aligning instead with the horizontal compressive axis. Although we do not quantify the fabric orientation, our detection of power oscillations from birefringent loss across all transect domains enabled us to conclude that the principal axes of the ice fabric (horizontal eigenvectors a_2 and a_3) within the upper ice column were generally not aligned parallel nor perpendicular to the ice stream margin. This statement may not hold for the entirety of the measured ice column because we do not know the vertical deformation profile that determines the proportion and orientation of lateral and longitudinal shear strain at any point in depth in comparison to rates measured at the surface. Notwithstanding this caveat, within the depth range that we observe birefringence loss, these findings are not only consistent with those made by Jordan, Martín, et al. (2020), but also support the influence of ice fabric on anisotropic rheology. Assuming that the ice at the center of the ESM embodies a non-ideal horizontal pole, the resulting fabric enhances shear deformation (Jackson & Kamb, 1997), in turn significantly "softening" the ice and enabling streaming flow (Minchew et al., 2018).

6. Discussion

6.1. On the Presence, Absence, and Detectability of Birefringence Patterns

Given theory (Sections 2.3 and 2.4), the presence of birefringence loss patterning is conditional upon (i) a sufficiently birefringent medium relative to radar frequency; and (ii) the antenna polarization plane aligned neither parallel nor perpendicular to the ice optic axis. Because the strain-induced rotation orients the

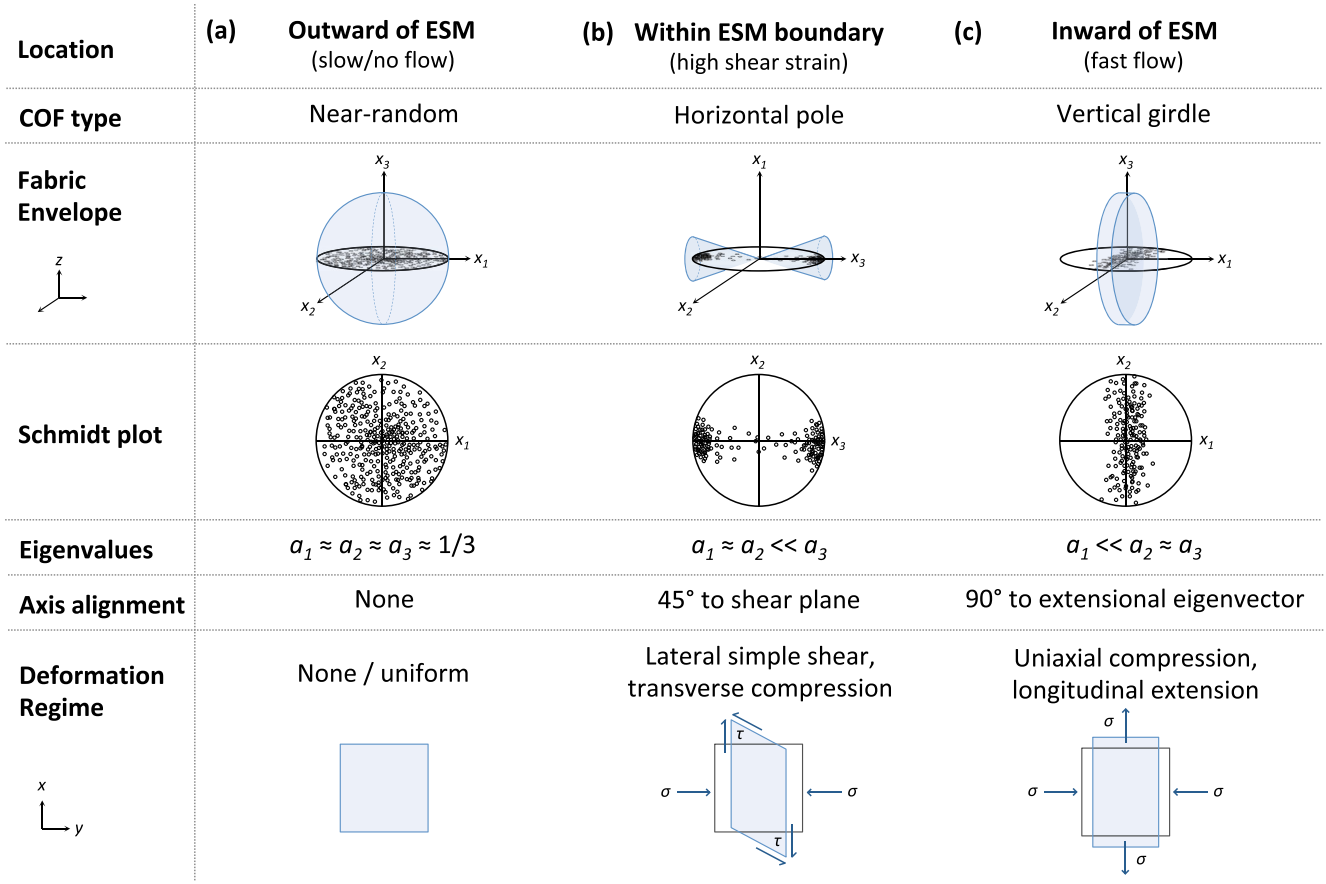

Figure 16. Schematic sample representation of COF development across the eastern shear margin (ESM) of Thwaites Glacier and the corresponding eigenvalues and deformation regimes leading to the observed COF, (a) outward of the ESM, (b) within the ESM boundaries, and (c) inward of the ESM as defined in Figure 12a. The fabric envelope and Schmidt plots show limiting cases (end-members) of the vertical girdle and horizontal pole models, where in reality we observe their non-ideal forms. The orientation of the eigenvectors (x_1, x_2, x_3) are specified with the vertical axis aligned with depth (z). The azimuthal fabric orientation with respect to Figure 15 is not specified. The schematics depicting each deformation regime are aligned along- (x) and across-flow (y), and show normal (σ) and shear (τ) stresses. The schematics show the original (white) and deformed (blue) states of a unit square, and do not show the vertical deformation tensors. COF, crystal orientation fabric; ESM, Eastern Shear Margin.

principal fabric axis toward the direction of maximum compression (Azuma & Higashi, 1985), the misalignment of the observed surface strain rate components with respect to the along-track direction of the flight transects (Figure 15a) amplifies the detection of birefringence that is manifested across the majority of the radargrams (Figures 6b–11b). In turn, the preferential alignment of ice crystals promotes streaming flow by enabling both enhanced shearing at the shear margins (Minchew et al., 2018; Pimienta et al., 1987) and compression inside the ice stream (Ma et al., 2010; Van der Veen & Whillans, 1994).

However, the delineation of birefringent minima only highlights patterning within the upper section (300–1,700 m) of the ice column. We were able to identify and trace more birefringent minima away from the center of the shear margin. These traces were observed at shallower depths within than outside the margin boundaries. The absence of periodic birefringence minima implies that the underlying fabric is either (i) azimuthally symmetric; or (ii) aligned at or close to the extinction planes ($\theta = 0°$, 90° in Figures 3a, 3c, 3g, and 3i) that mitigate the expression of birefringence-induced patterning.

Azimuthally symmetric fabrics are predicted to be present in the absence of any strain (resulting in isotropy), or as either a consequence of pure uniaxial vertical compression in the absence of convergent flow or a combination of rotation plus pure shear (both producing a vertical pole) (Alley, 1988). The former is expected in snow, firn, and young ice, although perturbations in climate are thought to induce slight crystal anisotropy at the near-surface (Kennedy et al., 2013). Even so, because weakly asymmetric ice would

induce long wavelengths of periodic birefringence loss, for example, a fabric asymmetry value of $\alpha = 0.05$ translates to a wavelength of ~400 m (Figure 5), it is likely that the absence of birefringence power minima in the uppermost sections of the ice column is a result of isotropic or near-isotropic ice. On the other hand, the latter is expected throughout the majority of the ice column at true ice domes (e.g., GRIP, Thorsteinsson et al., 1997) (Dome C, Durand et al., 2007; Durand et al., 2009) as well as the bottom reaches of ice divides where basal shear stresses dominate (e.g., Siple Dome, DiPrinzio et al., 2005) (WAIS Divide, Fitzpatrick et al., 2014). While we can certainly expect significant vertical shear on horizontal planes to be present as the result of basal drag within the ice stream interior close to the ice-bed interface (Blatter et al., 1998), the complex strain regime characterizing shear margins suggest a fabric history that is more complex than those observed at ice coring sites.

Because the Thwaites Glacier ESM is known to have weak basal control (MacGregor et al., 2013; Schroeder et al., 2016), it is plausible that the present-day direction of ice flow does not reflect its past ice flow regime. In particular, if we consider a probable scenario—that the spatial extent of the tributary was historically bounded by bed topography before migrating to its current tenuous position—both the shear margin and ice flow conceived from this configuration would then theoretically align at about 45° to the orientation of the radargram flight lines (Figure 4d). Given that the horizontal compression axis and the resulting near-surface fabric tend to also orient at 45° relative to the ice flow direction at ice stream margins (Jordan, Martín, et al., 2020), we would then expect no periodic power loss due to the co-alignment of the scenario's flow direction and the fabric eigenvectors with the azimuths that induce birefringent extinction. Although the time taken to overprint a pre-existing fabric is poorly constrained, evidence of remnant fabric at depth inconsistent with its contemporary flow regime suggest that it takes significant time to completely overwrite its history (Brisbourne et al., 2019; Lilien et al., in review). Therefore, a potential reorganization in ice flow of the tributary bounded by the ESM may explain the absence of birefringence-induced power loss in the lower half of the ice column (beyond 1,700 m).

Alternatively, the inability to detect birefringence loss outside this depth range may be a consequence of the radar received power being subjected to exponential geometric and scattering power fall-off (Haynes et al., 2018). At lower portions of the ice column (>2,000 m), the returned power observed in the radargrams approaches the noise floor. Although a low signal-to-noise ratio does not always correlate to a low polarimetric coherence (Jordan et al., 2019), here, the observed isotropy is likely not related to ice properties but instead should be regarded as a system limitation (K. Matsuoka et al., 2012). Moreover, the implied presence of an echo free zone in deeper ice within these radargrams (e.g., Drews et al., 2009) indicates a lack of reflector of any kind within this specified zone. Here, the lack of any signal power being scattered back to the receiving antenna likely prevents the radar from detecting any power variations whatsoever.

The delineated boundaries separating the vertical girdle and horizontal pole assumptions (Figure 12a) are arbitrarily binary and rather, the transitions between these two end members should instead be conceptualized as a continuum. The fabric that exists within this transition would likely be misaligned with depth and may also result in the disappearance and/or distortion of internal layering, the latter a reflection of the limitations of the polarimetric backscatter model used in this study. These two issues can potentially be addressed through modeling off-nadir wave propagation where none of the fabric eigenvectors are aligned with the vertical (K. Matsuoka et al., 2009; Jordan, Besson, et al., 2020), although these methods are considerably more complex.

Without a complete three-dimensional calculation of the strain regime, we were unable to predict the development of fabric asymmetry beyond our observations. Therefore, we only speculate on the presence or absence of azimuthal fabric anisotropy, and therefore birefringent power loss, outside the observed depths and areas. Notwithstanding this limitation, the presence of birefringence loss is ultimately a visual expression of the shear state of the eastern shear margin of Thwaites Glacier.

6.2. Model Sensitivity to Birefringence-Induced Power Loss

The detectability of birefringent layers also depends on the choice of parameters used in the polarimetric backscatter model to estimate fabric asymmetry from the wavelength of birefringence-induced power loss. Importantly, the amount of anisotropic scattering prescribed in our model dictates the relative azimuths

at which birefringence-induced power loss is most pronounced (Figure 3). In practice, anisotropic scattering boundaries typically occur with some amount of birefringence, and may lead to jump differences in rheology above and below the dividing layering (Eisen et al., 2007; Ross et al., 2020). Although we nominally prescribe a moderate amount of anisotropic scattering that is constant through depth ($R = 5$ dB) in our calculations of fabric strength from birefringence loss (Figure 5), our models do not take into account depth variations in anisotropic scattering. Anisotropic scattering is poorly constrained and difficult to measure, although optical observations indicate a correlation with birefringence and azimuthal fabric asymmetry over trapped air bubble morphology (Drews et al., 2012; Rongen et al., 2020). Our calculations show that the prominence of birefringent minima is independent of pattern amplitude and decreases with increasing fabric asymmetry (Figure S2a) as well as with system frequency (Figure S2b) and dielectric anisotropy (crystal birefringence) (Figure S2c). Additionally, its periodic amplitude becomes less prominent with increasing anisotropic scattering (Figures 3g–3i and S2d). While the difference between the end member cases result in a two-fold reduction in power, the theoretically predicted amount of periodic power loss with a high amount of prescribed anisotropic scattering ($R = 10$ dB) is still sufficiently large (15 dB) to be present in radargrams given ideal system settings and an adequately strong fabric.

6.3. Methodological Significance

The detection of birefringence-induced patterns uniformly observed across the ESM, and their spatial correlation with surface shear strain rates (Figure 15b), suggests that their presence is an expression of the deformation processes that gave rise to the observed fabric asymmetry at the shear margin. In this study, we investigated the presence of arch formations in airborne radar transects that, together with a peak in fabric strength centered about the location of maximum shear, delineate the extent of the Thwaites Glacier ESM (Figure 12). We would expect the links between the magnitude and orientation of shear strain, the periodicity of birefringent minima, and the azimuthal strength of fabric asymmetry shown in this study to also hold true for the imaged shear margins bounding the NEGIS, where similarly shaped birefringent layer arches were observed using a previous version of the CReSIS Accumulation Radar (Figure 1b). Because higher radar frequencies produce a shorter birefringence periodicity (a shorter wavelength of periodic birefringent minima) given the same measured bulk COF (Figure S2b), we would expect this phenomena to be more conspicuous in ice penetrating radars operating at the upper end of the frequency spectrum for ice-penetrating radars (>300 MHz) (Figure 6 in Fujita et al., 2006). This depth-frequency relationship can be qualitatively observed by visually comparing radargrams crossing the Thwaites ESM using two different radars, where the radargram produced using the higher-frequency Accumulation-C radar (750 MHz, Figure 1d and the subject of this manuscript) shows, in general, shorter birefringence periodicities with the depth of the first detected birefringent minima at a shallower depth than those produced using the lower frequency Multichannel Coherent Radar Depth Sounder (MCoRDS) radar (190 MHz, Figure 1a). However, given a sufficiently birefringent medium and appropriate instrument parameters, radar systems using frequencies markedly below this nominal threshold can still infer similar birefringence patterning, as shown in a 250 km-long transect across the Dome C domain imaged using the 60 MHz University of Texas High Capability Radar Sounder (HiCARS) system (Figure 1c and Table 1).

The Dome C radargram example (Figure 1c) also illustrates that the presence of birefringent patterning is not restricted to shear margins, but also to areas that exhibit different deformation regimes. In addition to dome flow, characterized by mild horizontal shear that progressively increases with depth (e.g., Durand et al., 2009), we also observed birefringent patterning in frames within the same flight line both earlier and later than the transects that cross the Thwaites ESM. Notable locations within this flight line (line 2 on 29 January 2019) include profiles aligned cross-flow to the trunk of Pine Island Glacier (frames 8 to 11) as well as profiles aligned along-flow to the trunk of Thwaites Glacier (frames 39 to 45). Our examples here and in Figure 1 are by no means exhaustive. Further analysis of birefringent patterning across a wider range of different strain regimes is warranted and undoubtedly will strengthen our argument that the observed power extinction patterns are birefringence-induced and is the subject of subsequent study.

Because the COF of polar ice is reflective of long-term strain history at timescales proportional to the ice age-depth relationship (e.g., Alley, 1988), the arcuate formations in our study, as a representation of cross-flow fabric anisotropy, are likely a physical manifestation of the rheological anisotropy of flow-induced fab-

ric that are produced under simple shear. As evidence of past streaming flow is likely to remain in its fabric signature on the order of 10,000 years (Lilien et al., in review), we conjecture that the similar arcuate-shaped birefringence pattern at lower depths between 15 and 20 km outside the shear margin center in Transect A represents a remnant of a past shear margin location that, given near stagnant flow (~1 m a^{-1}, Figure 6d) has yet to be completely overprinted. The location of this arch formation is almost coincident (offset by 1–2 km) with a steep 600+ m drop in bed elevation (Figure 4d), suggesting that, given the strong spatial control exerted by basal topography on the locations of shear margins, including the others delineating Thwaites Glacier (Holt et al., 2006; MacGregor et al., 2013; Raymond et al., 2001; Schroeder et al., 2016), the upper reaches of the ESM may have historically followed topographical boundaries within the confines of our study area. Although we do not attempt to provide temporal estimates, the proposition of inward shear margin migration to its present location is warranted from previous findings of weak topographic control along the upper reaches of the ESM that suggest its stability to be ephemeral relative to glaciological timescales (MacGregor et al., 2013; Schroeder et al., 2016). Changes in ice stream width can have significant consequences for ice discharge (Catania et al., 2006; Schoof, 2012) and motivates further analysis of potential shear margin migration at the Thwaites Glacier ESM.

Lastly, if this specific birefringent arch indeed represents the physical manifestation of a relic shear margin, the capability of airborne radar to locate present and potentially past shear margins purely through birefringence offers a novel and practical method to capture the dynamics of polar ice sheets over time. With regards to the present, the ability to detect hidden shear zones on ice shelves presents a complementary approach to current ground-penetrating radar methods (Arcone et al., 2016), which can be difficult to interpret due to the complexity of features such as intersecting crevasses and complex internal stratigraphy that complicate the resulting imagery (Kaluzienski et al., 2019). This may not only aid operational safety (Whillans & Merry, 2001), but also predict the spatial development of crevasse-damaged areas (Lhermitte et al., 2020). Regarding the past, the ability to reconstruct former shear margins may reveal valuable information regarding the genesis, evolution, and stagnation of deactivated ice streams (Catania et al., 2005; Conway et al., 2002; Jacobel et al., 2000; Retzlaff & Bentley, 1993), which leads to a better understanding of ice stream flow (Bougamont et al., 2003) and ice sheet stability (Catania et al., 2006).

7. Summary and Conclusions

It is well-known that shear margins are subject to fabric development, but their relationship is poorly quantified and incorporated into numerical ice flow models. Our study provides a powerful remote sensing method that images and estimates the underlying shear-induced fabric from airborne radargram profiles. Under the assumption that lateral variations in birefringence loss periodicity are a physical representation of variations in azimuthal fabric strength, we quantified the evolution of the crystal orientation fabric along six Accumulation-C radar transects crossing the eastern shear margin of Thwaites Glacier. At the center of the shear margin, we observed relatively strong azimuthal fabric anisotropy coincident with high shear strain that is consistent with behavior predicted by theoretical and experimental studies. This finding contrasts with observations on either side of the margin: outside the margin boundary where ice is stagnant, radar measurements infer the fabric to be near-isotropic, while on the other side of the boundary, the fabric is stronger but more variable, potentially a physical manifestation of the complex strain field approaching the shear margin from inside the ice stream. The ascent and descent of traced birefringent minima reflect the change in fabric strength across the present-day shear margin: periodic minima rising closer to the ice surface correlate with a fabric that is strengthening as a result of progressively increasing shear, and the converse reflect a movement toward isotropy with decreasing shear. Overall, the fabric at the eastern shear margin of Thwaites Glacier was observed to be strain-induced by ice flow.

A crucial aspect of our findings concerns the arcuate morphology of the traced birefringence minima that visually characterizes and bounds the shear margin in all six transects, as well as an additional section of Transect A significantly offset from the location of maximum shear strain, which we suggest to potentially be a relic shear margin. Because the deformational and rheological history of ice is preserved in its underlying fabric, the ability of airborne radar to locate present and potentially past shear margins purely through the identification of birefringent minima may be an important method in characterizing the rheologic and flow history of polar ice sheets. Birefringence-induced power loss has been observed on numerous other

occasions in other radar data sets over both the Greenland and Antarctic Ice Sheets, its manifestation a function of the frequencies of the specific radar system. Given that many radar data sets are open source, including that collected by the CReSIS Accumulation Radar spanning over a decade, significantly more rheological insight can potentially be gleaned from further data-driven analyses in birefringence loss and other radioglaciological artifacts.

Data Availability Statement

2018–2019 SAR-processed airborne radargrams from the CReSIS Accumulation-C radar over the Thwaites Glacier catchment were obtained as part of the International Thwaites Glacier Collaboration, the full data set which can be obtained from (https://data.cresis.ku.edu/data/accum/). Code used to calculate fabric asymmetry from consecutive minima was published through Young et al. (2020).

Acknowledgments
This work is ITGC Contribution No. ITGC-036 and is an output from the Thwaites Interdisciplinary Margin Evolution (TIME) project as part of the International Thwaites Glacier Collaboration (ITGC), supported by Natural Environment Research Council (NERC) research grant #NE/S006788/1 supporting T. J. Young and P. Christoffersen, and National Science Foundation (NSF) research grant #1739027 supporting S. M. Tulaczyk and D. M. Schroeder. Logistics for this project were provided by the NSF-U.S. Antarctic Program and NERC-British Antarctic Survey. R. Culberg is supported by a USA Department of Defense NDSEG Fellowship and N. L. Bienert is supported by an NSF Graduate Research Fellowship. The authors acknowledge the use of data from CReSIS generated with support from the University of Kansas, NASA Operation IceBridge grant NNX16AH54G, NSF grants ACI-1443053, OPP-1739003, and IIS-183820, Lilly Endowment Incorporated, and Indiana METACyt Initiative. The authors thank Carl Robinson, Thomas A. Jordan, and John D. Paden for the collection and processing of the CReSIS Accumulation-C radargrams as part of the Thwaites Glacier Aerogeophysical Survey. The authors thank Emma C. Smith for assistance in producing the fabric envelope plots in Figure 16. The authors are grateful to Carlos Martín, Aslak Grinsted, David Lilien, Nicholas Rathmann, and Olaf Eisen for insightful discussions on ice fabric and rheology. The authors would like to thank in particular Steven Arcone, as well as the Editor (Olga Sergienko), Associate Editor, and two other anonymous reviewers for their constructive comments that improved this paper.

References

Alley, R. B. (1988). Fabrics in polar ice sheets: Development and prediction. *Science*, *240*(4851), 493–495. https://doi.org/10.1126/science.240.4851.493

Arcone, S. A., Lever, J. H., Ray, L. E., Walker, B. S., Hamilton, G., & Kaluzienski, L. (2016). Ground-penetrating radar profiles of the McMurdo Shear Zone, Antarctica, acquired with an unmanned rover: Interpretation of crevasses, fractures, and folds within firn and marine ice. *Geophysics*, *81*(1), WA21–WA34. https://doi.org/10.1190/GEO2015-0132.1

Arnold, E., Leuschen, C., Rodriguez-Morales, F., Li, J., Paden, J., Hale, R., & Keshmiri, S. (2020). CReSIS airborne radars and platforms for ice and snow sounding. *Annals of Glaciology*, *61*(81), 58–67. https://doi.org/10.1017/aog.2019.37

Azuma, N. (1994). A flow law for anisotropic ice and its application to ice sheets. *Earth and Planetary Science Letters*, *128*(3–4), 601–614. https://doi.org/10.1016/0012-821X(94)90173-2

Azuma, N., & Higashi, A. (1985). Formation Processes of Ice Fabric Pattern in Ice Sheets. *Annals of Glaciology*, *6*, 130–134. https://doi.org/10.3189/1985aog6-1-130-134

Azuma, N., Wang, Y., Mori, K., Narita, H., Hondoh, T., Shoji, H., & Watanabe, O. (1999). Textures and fabrics in the Dome F (Antarctica) ice core. *Annals of Glaciology*, *29*, 163–168. https://doi.org/10.3189/172756499781821148

Bentley, C. R. (1975). Advances in geophysical exploration of ice sheets and glaciers. *Journal of Glaciology*, *15*(73), 113–135. https://doi.org/10.3189/S0022143000034328

Blatter, H., Clarke, G. K. C., & Colinge, J. (1998). Stress and velocity fields in glaciers: Part II. Sliding and basal stress distribution. *Journal of Glaciology*, *44*(148), 457–466. https://doi.org/10.3189/S0022143000001970

Bogorodskiy, V. V., Trepov, G. V., & Fedorov, B. A. (1970). On measuring dielectric properties of glaciers in the field. In *Proceedings of the international meeting on radioglaciology* (pp. 20–31). Lyngby.

Bouchez, J. L., & Duval, P. (1982). The fabric of polycrystalline ice deformed in simple shear: Experiments in torsion, natural deformation and geometrical interpretation. *Textures and Microstructures*, *5*(3), 171–190. https://doi.org/10.1155/TSM.5.171

Bougamont, M., Tulaczyk, S. M., & Joughin, I. P. (2003). Response of subglacial sediments to basal freeze-on 2. Application in numerical modeling of the recent stoppage of Ice Stream C, West Antarctica. *Journal of Geophysical Research*, *108*(B4), 2223. https://doi.org/10.1029/2002jb001936

Brisbourne, A. M., Martín, C., Smith, A. M., Baird, A. F., Kendall, J. M., & Kingslake, J. (2019). Constraining recent ice flow history at korff ice rise, West Antarctica, using radar and seismic measurements of ice fabric. *Journal of Geophysical Research: Earth Surface*, *124*(1), 175–194. https://doi.org/10.1029/2018JF004776

Budd, W. F. (1972). The development of crystal orientation fabrics in moving ice. *Zeitschrift für Gletscherkunde und Glazialgeologie*, *8*(1–2), 65–105.

Castelletti, D., Schroeder, D. M., Mantelli, E., & Hilger, A. (2019). Layer optimized SAR processing and slope estimation in radar sounder data. *Journal of Glaciology*, *65*(254), 983–988. https://doi.org/10.1017/jog.2019.72

Castelnau, O., Thorsteinsson, T., Kipfstuhl, J., Duval, P., & Canova, G. R. (1996). Modeling fabric development along the GRIP ice core, central Greenland. *Annals of Glaciology*, *23*, 194–201. https://doi.org/10.3189/S0260305500013446

Catania, G. A., Conway, H., Raymond, C. F., & Scambos, T. A. (2005). Surface morphology and internal layer stratigraphy in the downstream end of Kamb Ice Stream, West Antarctica. *Journal of Glaciology*, *51*(174), 423–431. https://doi.org/10.3189/172756505781829142

Catania, G. A., Scambos, T. A., Conway, H., & Raymond, C. F. (2006). Sequential stagnation of Kamb Ice Stream, West Antarctica. *Geophysical Research Letters*, *33*(14), L14502. https://doi.org/10.1029/2006GL026430

Conway, H., Catania, G., Raymond, C. F., Gades, A. M., Scambos, T. A., & Engelhardt, H. (2002). Switch of flow direction in an Antarctic ice stream. *Nature*, *419*, 465–467. https://doi.org/10.1038/nature01081

Culberg, R., & Schroeder, D. M. (2020). Firn clutter constraints on the design and performance of orbital radar ice sounders. *IEEE Transactions on Geoscience and Remote Sensing*, *58*(9), 6344–6361. https://doi.org/10.1109/TGRS.2020.2976666

Dall, J. (2010). Ice sheet anisotropy measured with polarimetric ice sounding radar. In *30th international geoscience and remote sensing symposium (IGARSS 2010)* (pp. 2507–2510). Honolulu, HI: IEEE.

Dall, J. (2021). Estimation of crystal orientation fabric from airborne polarimetric ice sounding radar data. In *40th international geoscience and remote sensing symposium (IGARSS 2020)* (pp. 2975–2978). Waikoloa, HI: IEEE.

DiPrinzio, C. L., Wilen, L. A., Alley, R. B., Fitzpatrick, J. J., Spencer, M. K., & Gow, A. J. (2005). Fabric and texture at Siple Dome, Antarctica. *Journal of Glaciology*, *51*(173), 281–290. https://doi.org/10.3189/172756505781829359

Doake, C. S. M. (1981). Polarization of radio waves in ice sheets. *Geophysical Journal International*, *64*(2), 539–558. https://doi.org/10.1111/j.1365-246X.1981.tb02682.x

Drews, R., Eisen, O., Steinhage, D., Weikusat, I., Kipfstuhl, S., & Wilhelms, F. (2012). Potential mechanisms for anisotropy in ice-penetrating radar data. *Journal of Glaciology*, *58*(209), 613–624. https://doi.org/10.3189/2012JoG11J114

Drews, R., Eisen, O., Weikusat, I., Kipfstuhl, S., Lambrecht, A., Steinhage, D., et al. (2009). Layer disturbances and the radio-echo free zone in ice sheets. *The Cryosphere*, *3*, 195–203. https://doi.org/10.5194/tc-3-195-2009

Durand, G., Gillet-Chaulet, F., Svensson, A., Gagliardini, O., Kipfstuhl, S., Meyssonnier, J., et al. (2007). Change in ice rheology during climate variations – Implications for ice flow modeling and dating of the EPICA Dome C core. *Climate of the Past*, *3*(1), 155–167. https://doi.org/10.5194/cp-3-155-2007

Durand, G., Svensson, A., Persson, A., Gagliardini, O., Gillet-Chaulet, F., Sjolte, J., et al. (2009). Evolution of the texture along the EPICA Dome C ice core. In T. Hondoh (Ed.), *Physics of ice core records II: Papers collected after the 2nd international workshop on physics of ice core records, held in Sapporo, Japan, 2–6 February 2007* (Vol. *68*, pp. 91–105). Sapporo, Japan: Hokkaido University Press.

Echelmeyer, K. A., Harrison, W. D., Larsen, C., & Mitchell, J. E. (1994). The role of the margins in the dynamics of an active ice stream. *Journal of Glaciology*, *40*(136), 527–538. https://doi.org/10.3189/S0022143000012417

Eisen, O., Hamann, I., Kipfstuhl, S., Steinhage, D., & Wilhelms, F. (2007). Direct evidence for continuous radar reflector originating from changes in crystal-orientation fabric. *The Cryosphere*, *1*(1), 1–10. https://doi.org/10.5194/tc-1-1-2007

Elsworth, C. W., Schroeder, D. M., & Siegfried, M. R. (2020). Interpreting englacial layer deformation in the presence of complex ice flow history with synthetic radargrams. *Annals of Glaciology*, *61*, 206–213. https://doi.org/10.1017/aog.2019.41

Ershadi, M. R., Drews, R., Martín, C., Eisen, O., Ritz, C., Corr, H., et al. (2021). Polarimetric radar reveals the spatial distribution of ice fabric at domes in East Antarctica. *The Cryosphere Discussions*, 1–34. https://doi.org/10.5194/tc-2020-370

Fitzpatrick, J. J., Voigt, D. E., Fegyveresi, J. M., Stevens, N. T., Spencer, M. K., Cole-Dai, J., et al. (2014). Physical properties of the WAIS divide ice core. *Journal of Glaciology*, *60*(224), 1181–1198. https://doi.org/10.3189/2014JoG14J100

Fujita, S., Maeno, H., & Matsuoka, K. (2006). Radio-wave depolarization and scattering within ice sheets: A matrix-based model to link radar and ice-core measurements and its application. *Journal of Glaciology*, *52*(178), 407–424. https://doi.org/10.3189/172756506781828548

Fujita, S., Matsuoka, T., Ishida, T., Matsuoka, K., & Mae, S. (2000). A summary of the complex dielectric permittivity of ice in the megahertz range and its applications for radar sounding of polar ice sheets. In T. Hondoh (Ed.), *Physics of ice core records* (pp. 185–212). Sapporo, Japan: Hokkaido University Press.

Gardner, A. S., Moholdt, G., Scambos, T., Fahnstock, M., Ligtenberg, S., van den Broeke, M., & Nilsson, J. (2018). Increased West Antarctic and unchanged East Antarctic ice discharge over the last 7 years. *The Cryosphere*, *12*(2), 521–547. https://doi.org/10.5194/tc-12-521-2018

Gillet-Chaulet, F., Gagliardini, O., Meyssonnier, J., Montagnat, M., & Castelnau, O. (2005). A user-friendly anisotropic flow law for ice-sheet modeling. *Journal of Glaciology*, *51*(172), 3–14. https://doi.org/10.3189/172756505781829584

Greene, C. A., Gwyther, D. E., & Blankenship, D. D. (2017). Antarctic mapping tools for MATLAB. *Computers & Geosciences*, *104*, 151–157. https://doi.org/10.1016/j.cageo.2016.08.003

Hansen, D. P., & Wilen, L. A. (2002). Performance and applications of an automated *c*-axis ice-fabric analyzer. *Journal of Glaciology*, *48*(160), 159–170. https://doi.org/10.3189/172756502781831566

Hargreaves, N. D. (1977). The polarization of radio signals in the radio echo sounding of ice sheets. *Journal of Physics D: Applied Physics*, *10*(9), 1285–1304. https://doi.org/10.1088/0022-3727/10/9/012

Hargreaves, N. D. (1978). The radio-frequency birefringence of polar ice. *Journal of Glaciology*, *21*(85), 301–313. https://doi.org/10.3189/s0022143000033499

Haseloff, M., Schoof, C., & Gagliardini, O. (2015). A boundary layer model for ice stream margins. *Journal of Fluid Mechanics*, *781*, 353–387. https://doi.org/10.1017/jfm.2015.503

Haynes, M. S., Chapin, E., & Schroeder, D. M. (2018). Geometric power fall-off in radar sounding. *IEEE Transactions on Geoscience and Remote Sensing*, *56*(11), 6571–6585. https://doi.org/10.1109/TGRS.2018.2840511

Hindmarsh, R. C. A. (2004). A numerical comparison of approximations to the Stokes equations used in ice sheet and glacier modeling. *Journal of Geophysical Research*, *109*(F1). https://doi.org/10.1029/2003JF000065

Holschuh, N., Christianson, K., & Anandakrishnan, S. (2014). Power loss in dipping internal reflectors, imaged using ice-penetrating radar. *Annals of Glaciology*, *55*(67), 49–56. https://doi.org/10.3189/2014AoG67A005

Holt, J. W., Blankenship, D. D., Morse, D. L., Young, D. A., Peters, M. E., Kempf, S. D., et al. (2006). New boundary conditions for the West Antarctic Ice Sheet: Subglacial topography of the Thwaites and Smith glacier catchments. *Geophysical Research Letters*, *33*(9). https://doi.org/10.1029/2005GL025561

Horgan, H. J., Anandakrishnan, S., Alley, R. B., Burkett, P. G., & Peters, L. E. (2011). Englacial seismic reflectivity: Imaging crystal-orientation fabric in West Antarctica. *Journal of Glaciology*, *57*(204), 639–650. https://doi.org/10.3189/002214311797409686

Jackson, M., & Kamb, B. (1997). The marginal shear stress of ice stream B, West Antarctica. *Journal of Glaciology*, *43*(145), 415–426. https://doi.org/10.3189/S0022143000035000

Jacobel, R. W., Scambos, T. A., Nereson, N. A., & Raymond, C. F. (2000). Changes in the margin of Ice Stream C, Antarctica. *Journal of Glaciology*, *46*(152), 102–110. https://doi.org/10.3189/172756500781833485

Jacobson, H. P., & Raymond, C. F. (1998). Thermal effects on the location of ice stream margins. *Journal of Geophysical Research*, *103*(B6), 12111–12122. https://doi.org/10.1029/98JB00574

Jiracek, G. R. (1967). Radio sounding of Antarctic ice. In *University of Wisconsin Geophysical and Polar Research Centre, Research Report Series No. 67–1* (pp. 1–127).

Jordan, T. M., Besson, D. Z., Kravchenko, I., Latif, U., Madison, B., Nokikov, A., & Shultz, A. (2020). Modeling ice birefringence and oblique radio wave propagation for neutrino detection at the South Pole. *Annals of Glaciology*, *61*(81), 84–91. https://doi.org/10.1017/aog.2020.18

Jordan, T. M., Martín, C., Brisbourne, A., Schroeder, D., & Smith, A. (2020). Radar characterization of ice crystal orientation fabric and anisotropic rheology within an Antarctic ice stream. *Earth and Space Science Open Archive*, 1–48. https://doi.org/10.1002/essoar.10504765.1

Jordan, T. M., Schroeder, D. M., Castelletti, D., Li, J., & Dall, J. (2019). A polarimetric coherence method to determine ice crystal orientation fabric from radar sounding: Application to the NEEM ice core region. *IEEE Transactions on Geoscience and Remote Sensing*, *57*(11), 8641–8657. https://doi.org/10.1109/tgrs.2019.2921980

Jordan, T. M., Schroeder, D. M., Elsworth, C. W., & Siegfried, M. R. (2020). Estimation of ice fabric within Whillans Ice Stream using polarimetric phase-sensitive radar sounding. *Annals of Glaciology*, *61*(81), 74–83. https://doi.org/10.1017/aog.2020.6

Jouzel, J., & Masson-Delmotte, V. (2010). Paleoclimates: What do we learn from deep ice cores? *WIREs Climate Change*, *1*(5), 654–669. https://doi.org/10.1002/wcc.72

Kaluzienski, L., Koons, P., Enderlin, E., Hamilton, G., Courville, Z., & Arcone, S. (2019). Crevasse initiation and history within the mcmurdo shear zone, antarctica. *Journal of Glaciology*, *65*(254), 989–999. https://doi.org/10.1017/jog.2019.65

Kennedy, J. H., Pettit, E. C., & Di Prinzio, C. L. (2013). The evolution of crystal fabric in ice sheets and its link to climate history. *Journal of Glaciology*, *59*(214), 357–373. https://doi.org/10.3189/2013JoG12J159

Kluskiewicz, D., Waddington, E. D., Anandakrishnan, S., Voigt, D. E., Matsuoka, K., & McCarthy, M. P. (2017). Sonic methods for measuring crystal orientation fabric in ice, and results from the West Antarctic ice sheet (WAIS) divide. *Journal of Glaciology*, *63*(240), 603–617. https://doi.org/10.1017/jog.2017.20

Kyrke-Smith, T. M., Katz, R. F., & Fowler, A. C. (2013). Stress balances of ice streams in a vertically integrated, higher-order formulation. *Journal of Glaciology*, *59*(215), 449–466. https://doi.org/10.3189/2013JoG12J140

Lewis, C. S. (2010). *Airborne UHF radar for fine resolution mapping of near surface accumulation layers in Greenland and West Antarctica (Unpublished master's thesis)*. University of Kansas.

Lhermitte, S., Sun, S., Shuman, C., Wouters, B., Pattyn, F., Wuite, J., et al. (2020). Damage accelerates ice shelf instability and mass loss in Amundsen Sea embayment. *Proceedings of the National Academy of Sciences of the United States of America*, *117*(40), 24735–24741. https://doi.org/10.1073/pnas.1912890117

Li, J., Vélez González, J. A., Leuschen, C., Harish, A., Gogineni, P., Montagnat, M., et al. (2018). Multi-channel and multi-polarization radar measurements around the NEEM site. *The Cryosphere*, *12*(8), 2689–2705. https://doi.org/10.5194/tc-12-2689-2018

Lilien, D. A., Rathmann, N. M., Hvidberg, C. S., & Dahl-Jensen, D. (in review). Modeling ice-crystal fabric as a proxy for ice-stream stability. *Journal of Geophysical Research: Earth Surface*, 1–37.

MacGregor, J. A., Catania, G. A., Conway, H., Schroeder, D. M., Joughin, I., Young, D. A., et al. (2013). Weak bed control of the eastern shear margin of Thwaites Glacier, West Antarctica. *Journal of Glaciology*, *59*(217), 900–912. https://doi.org/10.3189/2013JoG13J050

MacGregor, J. A., Fahnestock, M. A., Catania, G. A., Paden, J. D., Prasad Gogineni, S., Young, S. K., et al. (2015). Radiostratigraphy and age structure of the Greenland ice sheet. *Journal of Geophysical Research: Earth Surface*, *120*, 212–241. https://doi.org/10.1002/2014JF003215

Martín, C., Hindmarsh, R. C. A., & Navarro, F. J. (2009). On the effects of divide migration, along-ridge flow, and basal sliding on isochrones near an ice divide. *Journal of Geophysical Research*, *114*(F2), F02006. https://doi.org/10.1029/2008JF001025

Matsuoka, K., Furukawa, T., Fujita, S., Maeno, H., Uratsuka, S., Naruse, R., & Watanabe, O. (2003). Crystal orientation fabrics within the Antarctic ice sheet revealed by a multipolarization plane and dual-frequency radar survey. *Journal of Geophysical Research*, *108*(B10), 10. https://doi.org/10.1029/2003JB002425

Matsuoka, K., Power, D., Fujita, S., & Raymond, C. F. (2012). Rapid development of anisotropic ice-crystal-alignment fabrics inferred from englacial radar polarimetry, central West Antarctica. *Journal of Geophysical Research*, *117*(F3), F03029. https://doi.org/10.1029/2012JF002440

Matsuoka, K., Wilen, L., Hurley, S. P., & Raymond, C. F. (2009). Effects of birefringence within ice sheets on obliquely propagating radio waves. *IEEE Transactions on Geoscience and Remote Sensing*, *47*(5), 1429–1443. https://doi.org/10.1109/TGRS.2008.2005201

Matsuoka, T., Fujita, S., Morishima, S., & Mae, S. (1997). Precise measurement of dielectric anisotropy in ice Ih at 39 GHz. *Journal of Applied Physics*, *81*(5), 2344–2348. https://doi.org/10.1063/1.364238

Ma, Y., Gagliardini, O., Ritz, C., Gillet-Chaulet, F., Durand, G., & Montagnat, M. (2010). Enhancement factors for grounded ice and ice shelves inferred from an anisotropic ice-flow model. *Journal of Glaciology*, *56*(199), 805–812. https://doi.org/10.3189/002214310794457209

Meyer, C. R., & Minchew, B. M. (2018). Temperate ice in the shear margins of the Antarctic Ice Sheet: Controlling processes and preliminary locations. *Earth and Planetary Science Letters*, *498*, 17–26. https://doi.org/10.1016/j.epsl.2018.06.028

Meyer, C. R., Yehya, A., Minchew, B., & Rice, J. R. (2018). A Model for the Downstream Evolution of Temperate Ice and Subglacial Hydrology Along Ice Stream Shear Margins. *Journal of Geophysical Research: Earth Surface*, *123*(8), 1682–1698. https://doi.org/10.1029/2018JF004669

Minchew, B. M., Meyer, C. R., Robel, A. A., Gudmundsson, G. H., & Simons, M. (2018). Processes controlling the downstream evolution of ice rheology in glacier shear margins: Case study on Rutford Ice Stream, West Antarctica. *Journal of Glaciology*, *64*(246), 583–594. https://doi.org/10.1017/jog.2018.47

Montagnat, M., Azuma, N., Dahl-Jensen, D., Eichler, J., Fujita, S., Gillet-Chaulet, F., et al. (2014). Fabric along the NEEM ice core, Greenland, and its comparison with GRIP and NGRIP ice cores. *The Cryosphere*, *8*(4), 1129–1138. https://doi.org/10.5194/tc-8-1129-2014

Morlighem, M., Rignot, E., Binder, T., Blankenship, D., Drews, R., Eagles, G., et al. (2020). Deep glacial troughs and stabilizing ridges unveiled beneath the margins of the Antarctic ice sheet. *Nature Geoscience*, *13*(2), 132–137. https://doi.org/10.1038/s41561-019-0510-8

Peters, M. E., Blankenship, D. D., Carter, S. P., Kempf, S. D., Young, D. A., & Holt, J. W. (2007). Along-track focusing of airborne radar sounding data from West Antarctica for improving basal reflection analysis and layer detection. *IEEE Transactions on Geoscience and Remote Sensing*, *45*(9), 2725–2736. https://doi.org/10.1109/TGRS.2007.897416

Pimienta, P., Duval, P., & Lipenkov, V. Y. (1987). Mechanical behavior of anisotropic polar ice. In E. D. Waddington, & J. S. Walder (Eds.), *The physical basis of ice sheet modeling (proceedings of the Vancouver symposium, August 1987)* (Vol. 170, pp. 57–66). Wallingford, UK: International Association of Hydrological Sciences.

Qi, C., Prior, D. J., Craw, L., Fan, S., Llorens, M.-G., Griera, A., et al. (2019). Crystallographic preferred orientations of ice deformed in direct-shear experiments at low temperatures. *The Cryosphere*, *13*(1), 351–371. https://doi.org/10.5194/tc-13-351-2019

Raymond, C. F., Echelmeyer, K. A., Whillans, I. M., & Doake, C. S. M. (2001). Ice stream shear margins. In R. B. Alley, & R. A. Bindschadler (Eds.), *The West Antarctic ice sheet, behavior and environment* (pp. 137–155). Washington, DC, USA: American Geophysical Union. https://doi.org/10.1029/AR077

Retzlaff, R., & Bentley, C. R. (1993). Timing of stagnation of Ice Stream C, West Antarctica, from short-pulse radar studies of buried surface crevasses. *Journal of Glaciology*, *39*(133), 553–561. https://doi.org/10.3189/S0022143000016440

Rignot, E., Velicogna, I., Van Den Broeke, M. R., Monaghan, A., & Lenaerts, J. T. M. (2011). Acceleration of the contribution of the Greenland and Antarctic ice sheets to sea level rise. *Geophysical Research Letters*, *38*(5), L05503. https://doi.org/10.1029/2011GL046583

Riverman, K. L., Alley, R. B., Anandakrishnan, S., Christianson, K., Holschuh, N. D., Medley, B., et al. (2019). Enhanced firn densification in high-accumulation shear margins of the NE Greenland ice stream. *Journal of Geophysical Research: Earth Surface*, *124*(2), 365–382. https://doi.org/10.1029/2017JF004604

Rodriguez-Morales, F., Byers, K., Crowe, R., Player, K., Hale, R. D., Arnold, E. J., et al. (2014). Advanced multifrequency radar instrumentation for polar research. *IEEE Transactions on Geoscience and Remote Sensing*, *52*(5), 2824–2842. https://doi.org/10.1109/TGRS.2013.2266415

Rongen, M., Bay, R. C., & Blot, S. (2020). Observation of an optical anisotropy in the deep glacial ice at the geographic South Pole using a laser dust logger. *The Cryosphere*, *14*(8), 2537–2543. https://doi.org/10.5194/tc-14-2537-2020

Ross, N., Corr, H., & Siegert, M. (2020). Large-scale englacial folding and deep-ice stratigraphy within the West Antarctic ice sheet. *The Cryosphere*, *14*(6), 2103–2114. https://doi.org/10.5194/tc-14-2103-2020

Schoof, C. (2004). On the mechanics of ice-stream shear margins. *Journal of Glaciology*, *50*(169), 208–218. https://doi.org/10.3189/172756504781830024

Schoof, C. (2012). Thermally driven migration of ice-stream shear margins. *Journal of Fluid Mechanics*, *712*, 552–578. https://doi.org/10.1017/jfm.2012.438

Schroeder, D. M., Seroussi, H., Chu, W., & Young, D. A. (2016). Adaptively constraining radar attenuation and temperature across the Thwaites Glacier catchment using bed echoes. *Journal of Glaciology*, *62*(236), 1075–1082. https://doi.org/10.1017/jog.2016.100

Shepherd, A., Ivins, E., Rignot, E., Smith, B., van den Broeke, M., Velicogna, I., & Wouters, B. (2018). Mass balance of the Antarctic Ice Sheet from 1992 to 2017. *Nature*, *558*(7709), 219–222. https://doi.org/10.1038/s41586-018-0179-y

Smith, E. C., Baird, A. F., Kendall, J. M., Martín, C., White, R. S., Brisbourne, A. M., & Smith, A. M. (2017). Ice fabric in an Antarctic ice stream interpreted from seismic anisotropy. *Geophysical Research Letters*, *44*(8), 3710–3718. https://doi.org/10.1002/2016GL072093

Stockham, M., Macy, J., & Besson, D. (2016). Radio frequency ice dielectric permittivity measurements using CReSIS data. *Radio Science*, *51*(3), 194–212. https://doi.org/10.1002/2015RS005849

Suckale, J., Platt, J. D., Perol, T., & Rice, J. R. (2014). Deformation-induced melting in the margins of the West Antarctic ice streams. *Journal of Geophysical Research: Earth Surface*, *119*(5), 1004–1025. https://doi.org/10.1002/2013JF003008

Thorsteinsson, T., Kipfstuhl, J., & Miller, H. (1997). Textures and fabrics in the GRIP ice core. *Journal of Geophysical Research*, *102*(C12), 26583–26599. https://doi.org/10.1029/97JC00161

Thorsteinsson, T., Waddington, E. D., & Fletcher, R. C. (2003). Spatial and temporal scales of anisotropic effects in ice-sheet flow. *Annals of Glaciology*, *37*, 40–48. https://doi.org/10.3189/172756403781815429

Ulaby, F. T., Moore, R. K., & Fung, A. K. (1986). *Microwave Remote Sensing: Active and Passive*. Artech House.

Van der Veen, C. J., & Whillans, I. M. (1994). Development of fabric in ice. *Cold Regions Science and Technology*, *22*(2), 171–195. https://doi.org/10.1016/0165-232X(94)90027-2

Weikusat, I., Jansen, D., Binder, T., Eichler, J., Faria, S. H., Wilhelms, F., et al. (2017). Physical analysis of an Antarctic ice core-toward an integration of micro- and macrodynamics of polar ice. *Philosophical Transactions of the Royal Society A*, *375*(2086), 20150347. https://doi.org/10.1098/rsta.2015.0347

Whillans, I. M., & Merry, C. J. (2001). Analysis of a shear zone where a tractor fell into a crevasse, western side of the Ross Ice Shelf, Antarctica. *Cold Regions Science and Technology*, *33*(1), 1–17. https://doi.org/10.1016/S0165-232X(01)00024-6

Wilson, C. J. L., & Peternell, M. (2011). Evaluating ice fabrics using fabric analyzer techniques in Sørsdal Glacier, East Antarctica. *Journal of Glaciology*, *57*(205), 881–894. https://doi.org/10.3189/002214311798043744

Woodcock, N. H. (1977). Specification of fabric shapes using an eigenvalue method: Discussion. *Bulletin of the Geological Society of America*, *88*(9), pp. 1231–1236. https://doi.org/10.1130/0016-7606(1977)88<1231:sofsua>2.0.co;2

Woodruff, A. H. W., & Doake, C. S. M. (1979). Depolarization of radio waves can distinguish between floating and grounded ice sheets. *Journal of Glaciology*, *23*(89), 223–232. https://doi.org/10.1017/S0022143000029853

Young, T. J., Martín, C., Christoffersen, P., Schroeder, D. M., Tulaczyk, S. M., & Dawson, E. J. (2020). Rapid and accurate polarimetric radar measurements of ice crystal fabric orientation at the Western Antarctic Ice Sheet (WAIS) Divide deep ice core site. *The Cryosphere Discussions*, 1–22. https://doi.org/10.5194/tc-2020-264